Aerodynamic benefits of propeller-wing interactions in a leading edge distributed propeller configuration system

by

Kavin Balaji Saravanan

to obtain the degree of Master of Science
at the Delft University of Technology,
to be defended publicly on Thursday March 21, 2024 at 10:30 AM.

Student number:	5465346	
Thesis committee:	Prof. em. Dr. Ing. Georg Eitelberg,	TU Delft, Chairperson
	Dr. ir. Tomas Sinnige,	TU Delft, Supervisor
	Dr. Frits de Prenter,	Independent member
	ir. Robert Nederlof,	Additional member

An electronic version of this thesis is available at `http://repository.tudelft.nl/`.

SUMMARY

Propeller-based propulsion technology is experiencing renewed interest owing to its superior propulsive efficiency in comparison to conventional jet engines. This phenomenon is attributed to the capacity to generate thrust by accelerating a significant volume of air through a small velocity differential. Additionally, owing to its compatibility with electrical power systems, propeller-based propulsion offers an opportunity to utilize more environmentally friendly energy sources and configurations like the distributed propulsion systems. To optimize the integration between the propeller-based propulsion system and the airframe, it is imperative to thoroughly understand the interactive aerodynamics of the propeller-wing system.

This thesis presents a comprehensive study on the aerodynamics of propeller-wing interactions, with a specific focus on leading-edge distributed propeller configurations. The research was conducted through a comparative analysis, employing a single propeller-wing system, modeled based on the ATR 42/300 as the baseline. This involved comparing a conventional single tractor propeller configuration with a three-propeller leading-edge distributed configuration. The methodology used is an unsteady panel method solver, FlightStream, which is a commercially availabe software, allowing for an in-depth examination of the two-way interactions between the propeller and wing (Full interaction mode), and allowing for a force-free wake.

The solver is initially validated for its capacity to incorporate the effect of propeller swirl in the lift and drag distributions. This validation is essential as propeller swirl significantly influences the interactive aerodynamics of propeller-wing systems. employ the Kutta-Joukowski method for calculating the lift and induced drag distributions, as the surface pressure integration method demonstrated inaccuracies at low paneling densities. Further, the solver was validated against experimental results to ensure its suitability for addressing the developed research questions.

The findings of the study highlighted significant aerodynamic benefits of the leading-edge distributed propeller configuration over the traditional single propeller setup. Notably, there was a 2.5% increase in wing efficiency and a 6.1% reduction in induced drag. Additionally, the propeller efficiency in the distributed system saw a 3% increase compared to the single propeller system. However, it's crucial to note that these propellers operated at different, non-optimal points, which influences their comparative performance. A key result was the reduced power consumption of the three-propeller system, which required 8.1% less power to maintain steady level-flight conditions than the baseline single-propeller model. This finding suggests potential for increased efficiency in aircraft designs incorporating such configurations.

The thesis also offers several recommendations for future research in this field. A primary suggestion is the inclusion of the nacelle in the model, acknowledging its significant role in distributed propeller systems. This would offer a more complete understanding of the complexities within these systems. Additionally, the thesis advocates for expanding the scope of research to various distributed propeller configurations. Future studies could benefit from employing steady-state simulations with simplified propeller models, such as the Blade Element Momentum (BEM) theory or the actuator disc model, and exploring different arrangements and spacings between propellers.

CONTENTS

Summary i

List of Figures v

List of Tables vii

1 Introduction 1

2 Background 3
  2.1 Propeller aerodynamics . . . 3
    2.1.1 Propeller slipstream characteristics . . . 5
  2.2 Induced drag of the wing . . . 6

3 Propeller-Wing Interaction Aerodynamics 9
  3.1 Time-averaged effects of the propeller on wing aerodynamics . . . 9
    3.1.1 Influence of axial component of slipstream velocity . . . 9
    3.1.2 Influence of swirl component of slipstream velocity . . . 10
    3.1.3 Swirl recovery . . . 12
  3.2 Upstream effect of wing aerodynamics on propeller performance . . . 13
  3.3 Distributed propeller system . . . 14

4 Modeling techniques for propeller-wing interaction analysis 17
  4.1 Vortex lattice methods, Vortex panel methods, and higher order potential flow methods for propeller modeling . . . 17
  4.2 Wing modeling techniques . . . 18
    4.2.1 The Lifting-Line model. . . . 18
    4.2.2 Vortex Lattice Methods. . . . 20
    4.2.3 Vortex Panel Methods . . . 20
    4.2.4 Higher order methods . . . 22
  4.3 Propeller-wing interaction modeling techniques . . . 24
  4.4 Modeling viscous effects (corrections) . . . 26

5 Research outlook 29
  5.1 Gaps in literature . . . 29
  5.2 Research questions . . . 30

6 Methodology 31
  6.1 Geometry and mesh generation. . . . 31
  6.2 Aerodynamic analysis. . . . 31
    6.2.1 Panel methods . . . 33
    6.2.2 Viscous coupling. . . . 34
    6.2.3 Forces and moments. . . . 35

7 Validation 37
7.1 Initial validation . . . 37
7.1.1 Different methods to evaluate forces . . . 37
7.1.2 Capability of FlightStream to account for propeller swirl velocities. . . 39
7.2 Mesh refinement study . . . 43
7.2.1 Chordwise grid refinement study . . . 43
7.2.2 Spanwise grid refinement study . . . 44
7.3 Isolated propeller . . . 47
7.4 Isolated wing . . . 49
7.5 Validation of propeller-wing system. . . . 50

8 Results 53
8.1 Performance metrics for comparison . . . 54
8.2 Operating conditions . . . 54
8.2.1 Propeller operating point . . . 54
8.3 Single-propeller system . . . 55
8.3.1 Lift distribution . . . 55
8.3.2 Induced drag distribution . . . 56
8.3.3 System 1 vs. Isolated wing . . . 58
8.3.4 Propeller peformance in system 1 . . . 58
8.4 Multi-propeller system . . . 59
8.4.1 Lift distribution . . . 59
8.4.2 Induced drag distribution . . . 60
8.5 System 2 vs. Isolated wing. . . . 61
8.5.1 Propeller performance in system 2 . . . 62
8.5.2 System 1 vs. System 2 . . . 62

9 Conclusion and recomendations 65
9.1 Conclusion . . . 65
9.2 Recomendations for future work . . . 66

LIST OF FIGURES

2.1 Propeller force diagram for a blade section [5] 4
2.2 Propeller slipstream tube and vortex system [2] 5
2.3 Velocity variation in the spanwise and streamwise directions [7] 6
2.4 Lift distribution along a wing [1] 6
2.5 Reduction in effective AoA due to the downwash induced by the wing trailing vortcies [1] 7

3.1 Cl distribution over the wing behind the propeller due to axial velocity increase (The effect over the entire wing has not been shown purposely) [7] 10
3.2 Cl distribution over the wing behind the propeller due to swirl (The effect over the entire wing has not been shown purposely) [7] 11
3.3 Combined effect of axial and swirl components of slipstream velocity over the whole wing [7] 11
3.4 Tilting of the wing lift vector due to swirl-induced AoA [2] 12
3.5 Representation of induced velocities on an upstream propeller due to the wing [11] 14

4.1 Replacement of a finite wing by a horseshoe vortex [1] 19
4.2 Infinite number of horseshoe vortices superimposed to form a continuous lifting line [1] 19
4.3 Discretisation of lifting surface into elementary wings in VLM ([16]) 21
4.4 Comparison of C_L as a function of AoA for a NACA64A010 section with $AR = 3.0$, $\lambda = 0.5$, $\Lambda_{c/4} = 45°$ [16] 21
4.5 Composition of DVEs ([17]) 22
4.6 Comparison of the induced velocities by a fixed wake at the far field, as modeled by a lower order VLM vs using DVEs ([23]) 25

6.1 Wing and propeller cross sections used for generating surface mesh using the CCS method 32
6.2 Sample surface meshes generated using the CCS method 32
6.3 Relaxed wake of a wing [37] 34
6.4 iterative process for viscous coupling in FlightStream [39] 35

7.1 Comparison of different methods to calculate lift and drag distributions over the wingspan of a NACA0012 AR 10 wing at 5 deg AoA, Re = 2.8 Million 40
7.2 Comparison of Kutta-Joukowski method with and without viscous coupling to calculate lift and drag distributions over the wingspan of a NACA2412 AR 10 wing at 7 deg AoA, Re = 515,000 40

7.3 Tilting of the resultant force vector on either side of the propeller for a symmetric airfoil wing at $\alpha = 0°$ [7] . . . 41
7.4 Lift and drag distributions for a simple NACA0012 wing at 0 deg AoA with a leading-edge mounted propeller to ensure that swirl velocities are captured well . . . 42
7.5 Lift and drag distributions for a simple NACA0012 wing at 2 deg AoA with a leading-edge mounted propeller to ensure that induced drag is not completely 0 outside the slipstream boundaries . . . 42
7.6 Orthographic views of the propeller-wing setup used for validation [46] . . 43
7.7 Grid convergence test in the chordwise direction . . . 45
7.8 Grid convergence test in the spanwise direction . . . 46
7.9 TUD-XPROP propeller . . . 47
7.10 Validation of isolated propeller performance prediction . . . 48
7.11 Validation of the numerical model for prediction of integrated lift and drag polars (isolated wing) against experimental data [45] . . . 49
7.12 Validation of the numerical model for prediction of integrated lift and axial force polars (propeller-wing system) against experimental data [45] 50

8.1 Planform view of the two systems compared in this thesis . . . 53
8.2 Propeller operating point in System 1 and System 2 . . . 55
8.3 TUD-XPROP propeller . . . 57
8.4 Propeller operating point in system 1 and isolated propeller with same T_c 59
8.5 Multiple propeller system: Spanwise lift and drag distributions . . . 60
8.6 Illustration to show the effect of the adjacent propeller on the wing section behind an inboard propeller . . . 61
8.7 Propeller operating point in system 2 and isolated propeller with average T_C of the 3 propellers . . . 63

LIST OF TABLES

7.1 Chordwise grid convergence 44
7.2 Spanwise grid convergence 46
7.3 Performance parameters for isolated propeller 48

8.1 System 1 vs Isolated wing 59
8.2 System 1 Propeller performance 59
8.3 System 2 vs isolated wing 62
8.4 System 2 Propeller performance 63

1

INTRODUCTION

The pursuit of sustainable aviation has become a central goal in the aviation industry in recent years. This shift is primarily driven by the rising cost of fuel and a growing awareness of environmental issues. As a result, there is a reevaluation of the use of propeller-based propulsion systems due to their higher propulsive efficiencies compared to jet engines [1] and turbofan propulsion [2].

Additionally, propellers offer advantages in integrating with electrical power systems, which can facilitate more environmentally friendly and sustainable energy sources. It has been demonstrated that distributing smaller gas turbine engines across the aircraft's wingspan can enhance both propulsive and airframe structural efficiency. However, it's important to consider scaling effects, which may lead to lower thermal efficiencies. Scaling down the size of electric motors presents opportunities to improve the overall efficiency of aircraft.

Propeller-based propulsion systems provide the flexibility to explore concepts like distributed propulsion systems, as exemplified by NASA's X-57 Maxwell aircraft [3]. In this concept, leading-edge distributed propeller propulsion is combined with tip-mounted propellers in a puller configuration. This close integration between the propulsion system and the airframe opens avenues for innovative designs. Understanding the interaction between the propeller and the airframe is crucial for optimizing performance.

The flow behind a propeller exhibits higher axial momentum and added swirl, which affects surfaces in its slipstream, particularly the wing. The presence of the propeller influences the wing's aerodynamics, while the wing, in turn, impacts the propeller's performance. A tractor propeller can enhance the wing's lifting performance due to the higher axial momentum and increased angle of attack behind the upgoing blade side caused by swirl. Additionally, the aircraft's overall performance benefits from the swirl recovered from the propeller's slipstream through interaction with the wing [4]. Detailed discussions of these interactive phenomena are available in chapter 3

While computational fluid dynamics (CFD) and wind tunnel experiments are valuable tools for studying these interactions, they can be time-consuming and resource-intensive. Therefore, lower-order techniques like panel methods offer a more cost-effective approach for preliminary investigations. This thesis adopts a potential flow method-based unsteady panel method to conduct a comparative study between a single propeller-wing system and a distributed propeller-wing system. Unsteady panel methods strike a balance between fidelity and computational cost, allowing for the capture of interaction phenomena in full interaction mode (FIM), and wake relaxation to ensuring a force-free wake. Further details about the methodology are provided in Chapter chapter 6.

The necessary background information to comprehend the research motivation and questions outlined in Chapter chapter 5 is furnished in Chapter chapter 2. Research gaps, questions, methodology, validation, results, conclusions, and recommendations for future research are sequentially detailed in Chapters chapter 5, chapter 6, chapter 7, chapter 8, and chapter 9.

2

BACKGROUND

2.1. PROPELLER AERODYNAMICS

The propeller is a device that generates thrust by accelerating incoming air backwards through the rotation of blades around an axis. The cross-section of each blade conforms to an airfoil shape, thereby inducing a pressure differential between its front and rear surfaces. Consequently, the propeller experiences forces which can be segregated into two distinct components: thrust and torque, as illustrated in Figure 2.1

.

By utilizing Newton's third law, an equation can be established to describe the thrust generated by a propeller as a function of the rate of mass inflow to the propeller, the freestream velocity, and the jet velocity. This is shown in equation Equation 2.1. The propulsive efficiency, which is the ratio of propulsive power to the power imparted to the fluid (rate of change of kinetic energy of the fluid), can be calculated using equation Equation 2.2. The variable V_e denotes the outgoing jet velocity, while V_∞ represents the freestream velocity.

$$T = \dot{m}\left(V_e - V_\infty\right) \tag{2.1}$$

$$\eta_p = \frac{2}{1 + \dfrac{V_e}{V_\infty}} \tag{2.2}$$

To generate equivalent thrust, one approach involves accelerating a large mass of incoming air with a minimal velocity differential, or a small amount of incoming air can be accelerated by a large velocity differential. Equation 2.2 highlights that the propulsive efficiency of the propeller is greater when the velocity differential is minimized. Consequently, superior efficiencies are attained when a substantial mass of air is accelerated by a small increment. This explains why propellers typically exhibit higher propulsive efficiencies compared to jet engines. Jet engines, necessitating an outer cowling, are

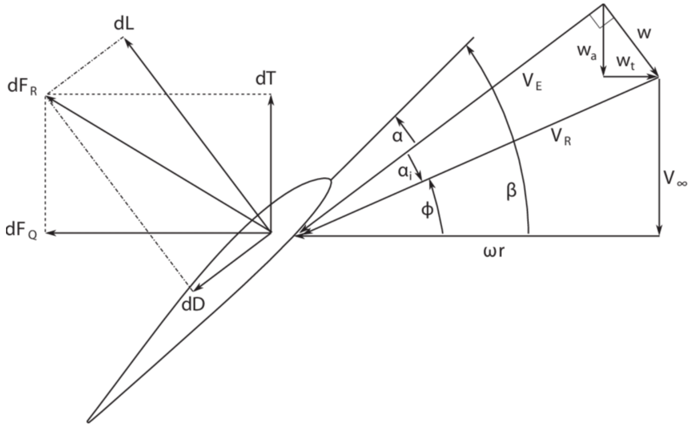

Figure 2.1: Propeller force diagram for a blade section [5]

typically smaller in size relative to propellers of equal weight. This additional cowling contributes to increased weight and drag [6]. Hence, propellers allow a larger inflow of air, thereby yielding greater propulsive efficiencies.

To compare the aerodynamic performance of different propellers, several non-dimensional performance parameters can be defined. Firstly, the thrust produced by the propeller, denoted by T, can be made non-dimensional in two ways: either using the rotational speed, n, the propeller diameter, D_P, and the freestream density, ρ_∞, as shown in Equation 2.3, or by using the freestream velocity, V_∞, instead of the propeller rotational speed, as depicted in Equation 2.4. Similarly, the propeller power and torque can be non dimensionalised as Equation 2.5 and Equation 2.6 respectively.

$$C_T = \frac{T}{\rho_\infty n^2 D_p^4} \tag{2.3}$$

$$T_C = \frac{T}{\rho_\infty V_\infty D_P^2} \tag{2.4}$$

$$C_P = \frac{P}{\rho_\infty n^3 D_p^5} \tag{2.5}$$

$$C_Q = \frac{Q}{\rho_\infty n^2 D^5} \tag{2.6}$$

Another non-dimensional parameter that plays a significant role in the discussion of propeller performance and propeller-wing interaction is the advance ratio. The advance ratio is used to non-dimensionalize the propeller rotational velocity using the freestream velocity as shown in Equation 2.7 [6]. Additionally, the advance ratio can be interpreted

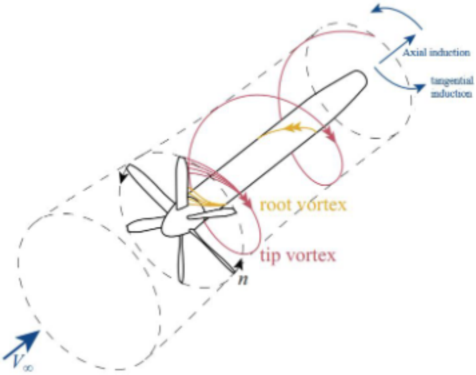

Figure 2.2: Propeller slipstream tube and vortex system [2]

as the distance covered by an aircraft during one revolution of its propeller.

$$J = \frac{V_\infty}{nD_p} \tag{2.7}$$

Now that C_T, C_P and J are defined, the propeller efficiency is given as Equation 2.8

$$\eta_p = \frac{C_T J}{C_P} \tag{2.8}$$

2.1.1. PROPELLER SLIPSTREAM CHARACTERISTICS

In order to describe the interactive flow around propeller-wing configurations, it is essential to understand the characteristics of the slipstream in the presence of the wing. As an initial starting point, the characteristics of the isolated propeller are discussed in this subsection. An intuitive way to look at a propeller is the concept of an advancing and rotating wing as shown in Figure 2.2.

AXIAL AND SWIRL VELOCITY PROFILES

The axial velocity component represents the velocity component that is parallel to the thrust axis of the propeller. In the blade's spanwise direction, there are significant gradients of axial velocity due to non-uniform loading along the blade. Typically, the maximum axial velocity value occurs around the $3/4R$ location, where R denotes the propeller radius. As the blade loading is minimal near the root and tip, the axial velocity is also at its minimum at these locations, as depicted in Figure 2.3a. The axial velocity in the slipstream increases as one moves further away from the propeller due to contraction (Figure 2.3b). This increase in axial velocity in the slipstream with increasing distance is crucial in propeller-wing interaction when considering the effect of the streamwise location of the propeller with respect to the wing.

In addition to the increase in axial velocity, the rotation of the propeller introduces an extra azimuthal component of velocity. The typical swirl velocity profile along the blade's

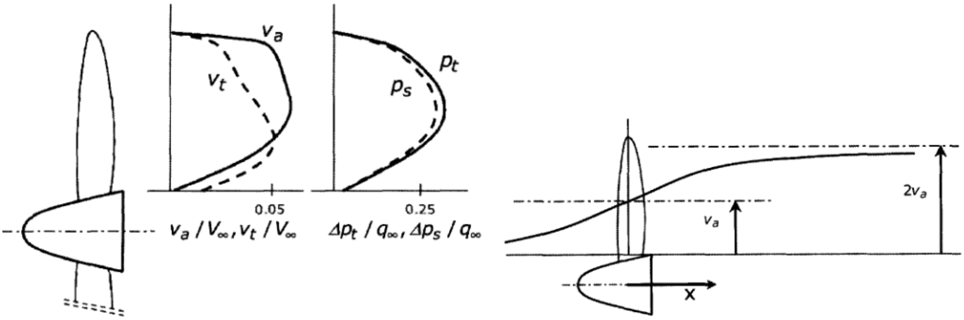
v_a
v_t
p_t
p_s
0.05
0.25
$v_a / V_\infty, v_t / V_\infty$
$\Delta p_t / q_\infty, \Delta p_s / q_\infty$
$2v_a$
v_a
x

(a) Typical axial and tangential velocity profiles along a blade

(b) Streamwise variation of slipstream axial velocity

Figure 2.3: Velocity variation in the spanwise and streamwise directions [7]

spanwise direction (V_t / V_∞) is depicted in Figure 2.3a. The tangential component of velocity plays a crucial role in the analysis of propeller-wing interactions as it changes the local angle of attack experienced by the wing. This is discussed in greater detail in subsection 3.1.2

2.2. INDUCED DRAG OF THE WING

The finite nature of a three-dimensional (3-D) wing causes the airflow to curl around the wingtips due to pressure differences between the upper and lower surfaces. This curling phenomenon results in the formation of wingtip vortices, which are most pronounced at the tips but are also weakly present across the entire wingspan [8]. As a consequence of the finite dimensions of a 3-D wing, there is a variation in the lift distribution along the wing. The lift distribution on a finite 3-D wing is presented in Figure 2.4 Consequently, this leads to a non-uniform circulation distribution along the wing, as the circulation at a given spanwise station is inherently linked to the lift per unit span at that particular station.

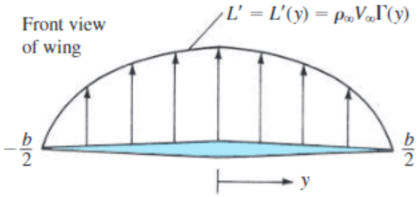

Figure 2.4: Lift distribution along a wing [1]

According to Helmholtz's vortex theorem, the variation in circulation along the wing results in the shedding of trailing vortices into the wake. These vortices, in turn, create a downwash effect on the wing, causing a reduction in the effective angle of attack seen by the wing. Thus, the local relative flow is now inclined by an angle α_i (Figure 2.5). The local lift vector is invariably perpendicular to the local flow direction, causing it to tilt backward and generate a component of the resultant force in the direction of V_∞. This component contributes to the drag and is known as induced drag. In the following sections, the impact of the propeller on the lift distribution will be discussed, as well as how this affects the induced drag [1].

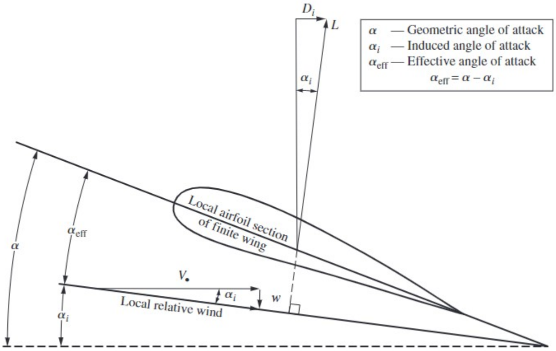
D_i
L
α — Geometric angle of attack
α_i — Induced angle of attack
α_{eff} — Effective angle of attack
$\alpha_{\text{eff}} = \alpha - \alpha_i$
α_i
α
α_{eff}
Local airfoil section of finite wing
V_∞
α_i
w
Local relative wind
α_i

Figure 2.5: Reduction in effective AoA due to the downwash induced by the wing trailing vortcies [1]

The influence of propeller slipstream velocities on the lift distribution of the wing, and consequently, on the induced drag of the wing, is addressed in section 3.1. The discussion will focus on explaining how the presence of the propeller modifies the lift distribution, and subsequently, how this modification impacts the induced drag of the wing.

3

PROPELLER-WING INTERACTION AERODYNAMICS

Propeller-wing interaction refers to the effect that the rotation of a propeller (propeller slipstream) has on the aerodynamics of an aircraft's wing and vice-versa. In this study, the investigation is specifically focused on aircraft configurations featuring leading-edge placed propellers in a puller arrangement. section 2.2 introduces fundamental concepts of wing lift distribution and induced drag, providing essential groundwork. section 3.1 discusses the influence of the propeller slipstream on the aerodynamics of the wing. The effect of the wing on the propeller loading is explained in section 3.2. Further, the effect of the propeller position relative to the wing is described in **??**.

3.1. TIME-AVERAGED EFFECTS OF THE PROPELLER ON WING AERODYNAMICS

In a tractor-propeller configuration, a portion of the wing lies in the propeller slipstream. This slipstream influences the flow over the wing and modifies its aerodynamic behavior. The propeller slipstream comprises two components: The axial component and the rotational component (swirl). Each of these components has its own distinct influence on the wing lift distribution, which in turn affects the induced drag and hence the aerodynamic performance of the wing. subsection 3.1.1 discusses the effects of the axial component and subsection 3.1.2 expands on the effects of the swirl component on wing aerodynamics. Furthermore, the concept of swirl recovery is also treated in subsection 3.1.3.

3.1.1. INFLUENCE OF AXIAL COMPONENT OF SLIPSTREAM VELOCITY

The propeller produces thrust by adding momentum to the flow. The blades of the propeller are designed such that they add energy to the flow. This additional momentum results in an increase in axial flow velocity in the slipstream of the propeller. Thus, the axial component of velocity in the slipstream is higher than the free stream velocity. This results in an increase in local lift and drag coefficients (when normalized using free-stream velocity) in the regions of the wing immersed in the slipstream (Figure 3.1). When the propeller thrust axis aligns with the free stream, the axial velocity distribution symmetrically aligns with the propeller thrust axis. Consequently, the effect on wing loading due to the axial component of the slipstream remains consistent on both the upgoing and downgoing blade sides of the wing. As a result, a symmetric increase in local lift occurs behind both the upgoing and downgoing blade sides, attributable to the symmetric rise in axial velocity over these regions. This phenomenon is illustrated in Figure 3.1. The alteration in local lift induces a corresponding change in local circulation. According to Helmholtz's vortex theorem, this variation in circulation along the wing prompts the shedding of trailing vortices into the wake, thereby inducing downwash velocities across the entire wingspan. Consequently, this modifies the lift distribution over the entire wingspan, extending beyond the slipstream-washed region.For the sake of simplicity, the change effect of the axial component over the whole wing is purposefully neglected in Figure 3.1.

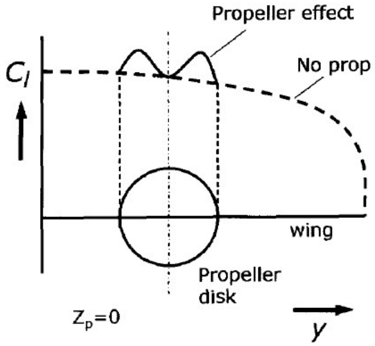

Figure 3.1: Cl distribution over the wing behind the propeller due to axial velocity increase (The effect over the entire wing has not been shown purposely) [7]

3.1.2. INFLUENCE OF SWIRL COMPONENT OF SLIPSTREAM VELOCITY

The phenomenon of propeller swirl refers to the tangential velocity component of the slipstream generated by a rotating propeller. This swirling motion induces an upwash behind the up-going blade side and a downwash behind the down-going blade side. Consequently, the effective angle of attack experienced by the wing on either side of the propeller thrust axis is altered. For instance, in the case of an inboard-up rotating propeller, the inboard side of the wing experiences an increase in the local effective angle of attack, while the outboard side experiences a decrease in the local effective angle of attack [7]. This results in an increase in the local lift coefficient on the inboard side and a decrease in the local lift coefficient on the outboard side, as illustrated in Figure 3.2. It should be noted that the local changes in the lift coefficient affect the entire lift distribution over the wing, as explained in subsection 3.1.1. However, for simplicity, only the local changes in lift distribution, over the slipstream washed region of the wing are emphasized in Figure 3.2. Thus, the swirl has an anti-symmetric effect on the wing lift distribution. Due to its anti-symmetric nature, the swirl dictates the combined influence of the propeller slipstream on the wing [7]. The combined effect of the propeller slipstream on the wing is shown in Figure 3.3.

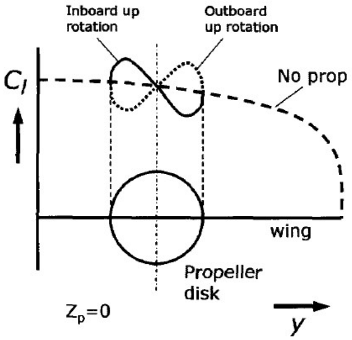

Figure 3.2: Cl distribution over the wing behind the propeller due to swirl (The effect over the entire wing has not been shown purposely) [7]

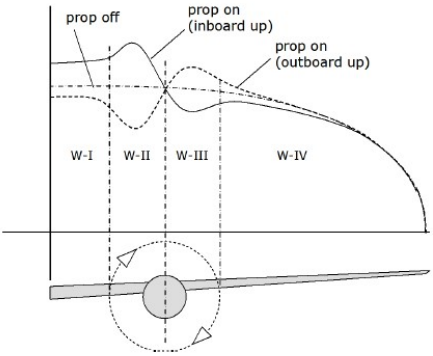

Figure 3.3: Combined effect of axial and swirl components of slipstream velocity over the whole wing [7]

In addition to modifying wing lift distribution, swirl also affects the induced drag of a wing. The upwash behind the upgoing blade side and downwash behind the downgoing blade side causes the resultant force vector to tilt forward and backward, respectively (see Figure Figure 3.4). As a result, there is a component of the lift vector that contributes to the drag (thrust) of the wing. The lift vector behind the upgoing blade side rotates forward, generating thrust (negative drag), while the opposite is true for the down-going blade side, where an increase in induced drag is present [7]. Consequently, both the

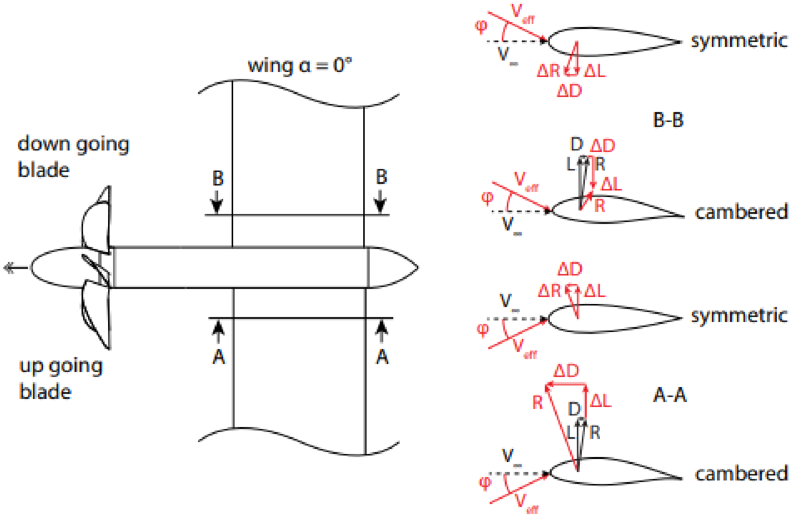

Figure 3.4: Tilting of the wing lift vector due to swirl-induced AoA [2]

lift and drag forces are influenced by the swirl component present in the propeller slipstream. Notably, swirl recovery, a net negative impact on the wing-induced drag, can be observed, which is discussed further in subsection 3.1.3. Therefore, both lift and drag forces are affected by swirl, with the net negative effect on wing-induced drag being of particular interest.

3.1.3. SWIRL RECOVERY

Another aspect to consider when studying these interactions is the reduction in rotational velocity in the slipstream caused by the wing's presence. Several studies have highlighted a significant reduction in rotational velocity in the slipstream due to the wing's presence. According to [4], the change in slipstream helix angle resulting from the wing-induced upwash and downwash in front and behind the wing, respectively, is the primary cause of this reduction in rotational velocity.

The interaction between the propeller and wing affects the induced drag. The forward rotation of the lift vector behind the upgoing blade side results in induced thrust, leading to a reduction in induced drag. Conversely, behind the downgoing blade side, the local lift vector tilts backward, amplifying induced drag. However, due to an increase in local angle of attack (AoA) behind the upgoing blade side and a decrease in local AoA behind the downgoing blade side, the lift vector is amplified and rotated forward behind the upgoing blade side, while it is attenuated and rotated backward behind the downgoing blade side. Consequently, the net effect of the propeller on the induced drag of the wing is negative and the wing is said to "recover swirl" [7].

Kroo et al.[9] conducted an analysis of various propeller wing configurations in inviscid incompressible flow to determine an optimal propeller wing integration with minimal induced loss. The study found a notable deviation from an elliptical load distribution, which is known to be the optimal load distribution for an isolated wing. The reason for this difference is attributed to the reduction in swirl recovery caused by the nearly equal magnitude of the backward and forward-rotated lift vector on either side of the propeller thrust axis when employing an elliptical load distribution. The study also suggests that with an appropriate wing lift distribution, the wing is capable of restoring much of the losses associated with slipstream swirl, claiming that in certain cases the propeller-wing interaction benefits can make such configurations more efficient than counter-rotating systems.

3.2. UPSTREAM EFFECT OF WING AERODYNAMICS ON PROPELLER PERFORMANCE

As discussed in section 2.2, lift is intricately connected to circulation in. Circulation, generated by the flow, produces lift on the wing. Importantly, this circulation induces velocities on the propeller if the propeller is placed within the range of the wing.

This induced velocity manifests in two distinct components: an axial velocity component and a tangential velocity component, often referred to as upwash. The tangential velocity component remains relatively constant across the entire span of the propeller and can be conceptualized as an effective increase in the angle of attack experienced by the propeller [10]. However, the axial velocity component exhibits a more intricate behavior. It results in an increase in the axial inflow velocity above the leading edge of the wing and a reduction in the axial velocity below the leading edge of the wing. This variance in axial inflow velocity has consequences: the portion of the propeller positioned above the wing's leading edge experiences reduced thrust, while the portion below the wing generates greater thrust. This disparity in thrust production leads to a nose-up pitching moment. A similar non-uniform loading and resultant yawing moment occurs in the direction of the upgoing blade side. As the upgoing blade moves into the upwash, it encounters a decrease in dynamic pressure, which results in decreased thrust production. Conversely, the downgoing blade experiences the opposite effect [11].

Another mechanism through which the wing exerts an influence on the upstream propeller's performance is known as the blockage effect. This effect arises as the wing presence increases the static pressure ahead of the wing, subsequently reducing the inflow velocity experienced by the propeller. This reduction in inflow velocity, in turn, leads to a decrease in the advance ratio at which the propeller operates, resulting in an increase in thrust [11].

Illustrating this concept, Figure 3.5 provides a diagram depicting how the wing induces the blockage effect on the propeller. In cases involving tip-mounted propellers, it's important to note that the blockage-induced axial velocities are most pronounced in the area where the wing is positioned behind the propeller. This, once again, results in a yawing moment, but this time toward the inboard direction.

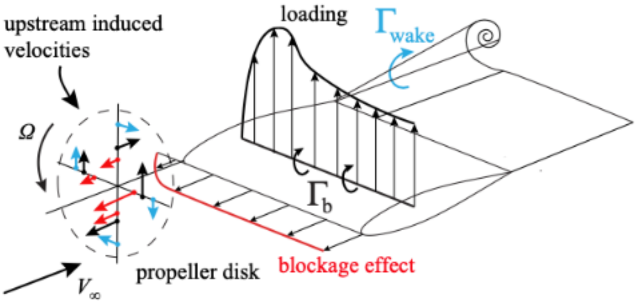

Figure 3.5: Representation of induced velocities on an upstream propeller due to the wing [11]

Furthermore, when a tip-mounted propeller operates in the inboard-up configuration, the wake generated by the wing contributes to the roll-up of the wing's wake, consequently diminishing the dynamic pressure within the upgoing blade side region. This complex interplay further adds to the multifaceted dynamics of propeller-wing interactions [11].

3.3. DISTRIBUTED PROPELLER SYSTEM

Lei et al. [12] investigated the performance of distributed electric propeller (DEP) systems numerically using RANS equations and wind tunnel tests, in a low Reynolds number regime. The major findings from this study were that the presence of DEP systems along the leading edge of the wing significantly improved the overall lift to drag ratio of the system. Additionally, it was also obtained that the relative position of the DEP system also played a role in the overall performance of the system. Interestingly, it was found that both lift and drag increased for all test cases, and the magnitude of increase depended on the angle of attack as well as the relative spacing of the DEP structure. They found that until an angle of attack of 16°, there was no significant effect of the DEP structure on the wing performance. After 16°, quite a noticeable increase in wing performance was seen. This is because the increase in axial velocity in the propeller slipstream over the wing delays the laminar flow separation, thus increasing the stall AoA. It was also concluded that there was a significant increase in thrust for the DEP system due to the blocking effect of the wing [12]. This study, however, had a shortcoming that the DEP system used for this study was a counter-rotating system, which would reduce the impact of propeller swirl recovery, which explains the negligible difference in wing performance in the linear range of AoAs. Moreover, there was no metric defined to evaluate the performance of the whole system together. It may happen that the increase in lift to drag ratio of the DEP system is negated by a corresponding decrease in propeller performance.

An experimental study conducted by [13] examined propeller-wing interactions in a distributed propeller propulsion system using a wind tunnel model. The study utilized a wing section with three co-rotating propellers, such that easy adjustment of the relative position between the wing and the propeller system was possible. Operating conditions for the study were set at $Re = 2.1 \times 10^6$ and $J = 0.65$. The study revealed that the maximum lift gain was achieved when the propeller was positioned at $x_P/c = -0.25$ or closer to the wing. Conversely, for optimal performance during takeoff, a greater separation distance ($x_P/c = -0.46$) between the propeller and the wing was found to be most advantageous. It's important to note that this study primarily investigated the influence of the streamwise location of the DEP system on lift gains alone. It did not specifically assess the performance benefits on the overall system using any particular metric to evaluate the effect on system performance.

A high fidelity numerical method was used by [14] to evaluate the aero-propulsive effects of a distributed propeller array on a UAV wing model. The research assessed the impact of varying propeller array positions, flap configurations of the wing, and AoA on the aeropropulsive effects for a UAV incorporating a distributed propulsion system. The study shows that the use of distributed propellers increases the lift, drag and pitching moment coefficients. The magnitude of this increase in these coefficients depends on the relative position of the propeller array, AoA, and the flap configuration. While the increase in lift is indeed a positive effect on the system, it is important to note that it was accompanied by an increase in drag and pitching moment. Once more, in this study, the emphasis was primarily on examining the influence of the distributed propeller system on wing performance, without defining a specific metric for comparing overall system performance. Furthermore, comparing the slipstream-blown wing to the unblown wing may have been unfair, as flight conditions differed between the two states.

There is no study that makes a fair comparison between a single propeller system and a distributed propeller system. The above mentioned studies also indicate that there is a need to establish a metric to evaluate the overall system performance. A fair comparison between a single propeller system and a distributed propeller system would enable the better understanding of distributed propeller systems and further parametric studies will help maximize interactive benefits.

4

MODELING TECHNIQUES FOR PROPELLER-WING INTERACTION ANALYSIS

4.1. VORTEX LATTICE METHODS, VORTEX PANEL METHODS, AND HIGHER ORDER POTENTIAL FLOW METHODS FOR PROPELLER MODELING

Vortex lattice methods (VLM) and vortex panel methods (VPM) belong to a class of potential flow modeling techniques that utilize vortex elements to represent both the lifting surface and the wake. Detailed explanations of these methods can be found in subsection 4.2.2 and subsection 4.2.3. Although these sections primarily discuss the application of these methods to wings, they can be adapted in a similar manner to model propellers and their wakes. These methods prove highly valuable for assessing the performance characteristics of an isolated propeller, as mentioned by Kooij [8].

However, the challenge arises when applying traditional VLM and VPM to study propeller-wing interactions. These methods are rooted in a fixed wake (frozen wake) formulation, where the shape of the propeller wake remains constant. In reality, the shape of the propeller wake is influenced by wing aerodynamics, and conversely, the wing's behavior is affected by the propeller wake. The interaction between a propeller and a wing is inherently unsteady. Consequently, a time-dependent free wake model becomes essential to investigate the two-way interaction between them, referred to as full interaction mode (FIM), as emphasized by Veldhuis [4]. Additionally, questions are raised regarding the suitability of VLM for propellers when the propeller wake interacts with another body or wake system, as discussed in [15].

To address the complexities of propeller-wing interactions, higher-order free wake methods have been developed, and these are elaborated on in the subsequent sections of this report, particularly in subsection 4.2.4.

4.2. WING MODELING TECHNIQUES

In this section, the analysis methods developed by various studies for modeling a wing and its wake in isolation, without being influenced by the presence of the propeller slipstream, are comprehensively examined. The scope of analysis methods presented here is confined to those rooted in potential flow techniques. subsection 4.2.1 provides a detailed exploration of the lifting line model, followed by an in-depth discussion of Vortex Lattice Methods (VLM) in subsection 4.2.2. Moving forward, subsection 4.2.3 is dedicated to Vortex Panel Methods (VPM), with the final section (subsection 4.2.4) delving into higher-order free wake methods. These higher-order methods are thoroughly investigated to elucidate how they address the limitations inherent in traditional VLMs and VPMs, as will be further elaborated upon in subsequent sections of this report, particularly in the context of wing modeling techniques and propeller-wing interaction analysis.

4.2.1. THE LIFTING-LINE MODEL

According to Prandtl, a vortex filament bound to a certain location in space produces a lift force, the magnitude of which can be estimated using the Kutta-Joukowski theorem. Thus, in theory, an infinite wing can be replaced with an equivalent bound vortex with the same circulation as that of the wing. For a finite wing, however, a bound vortex alone will not suffice due to Helmoltz's theorem which states that a vortex filament cannot start and end in a fluid. Thus, the vortex filament bends at the wingtips to continue downstream as two free trailing vortices to infinity. The bound vortex along with the two trailing vortices is known as a "Horseshoe vortex". Hence, a finite wing can be modeled as an equivalent horseshoe vortex.

The bound vortex filament induces no velocity along itself but the two trailing vortex filaments induce an upwash w at a given spanwise location y (refer Figure 4.2) given by Equation 4.1. From Equation 4.1, it is evident that the induced upwash velocity tends to ∞ at the wing tips.

$$w(y) = -\frac{\Gamma}{4\pi}\frac{b}{(b/2)^2 - y^2} \tag{4.1}$$

In order to avoid this issue of induced velocities approaching infinity at the wingtips, the finite wing is represented using multiple bound vortex filaments and their corresponding trailing vortex filament pair. Thus, the wing is now modeled by a system of horseshoe vortices. For an unswept wing, all the bound vortex filaments are coincident along the same line, known as the lifting line. An example of a lifting line composed of three superimposed horseshoe vortices is shown in Figure 4.2. The vortex strength of each trailing vortex filament is equal to the spanwise differential in circulation.

This concept is then extended to superimpose an infinite number of horseshoe vortices on the lifting line. The circulation $\Gamma(y)$ then becomes a continuous distribution

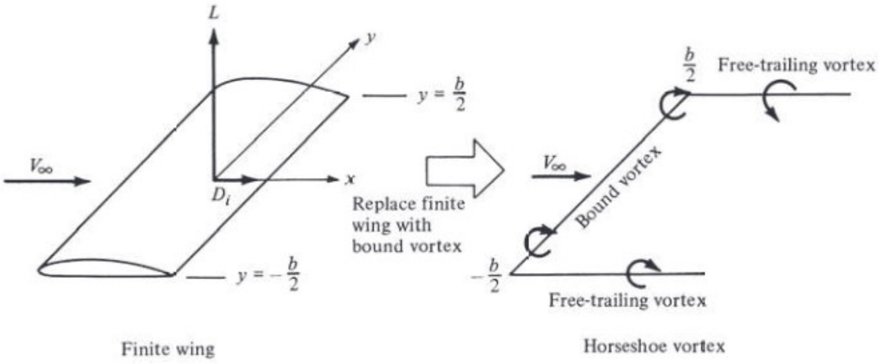
L
y
y = b/2
V∞
x
D_i
y = −b/2
Replace finite wing with bound vortex
b/2
Free-trailing vortex
V∞
Bound vortex
−b/2
Free-trailing vortex
Finite wing
Horseshoe vortex

Figure 4.1: Replacement of a finite wing by a horseshoe vortex [1]

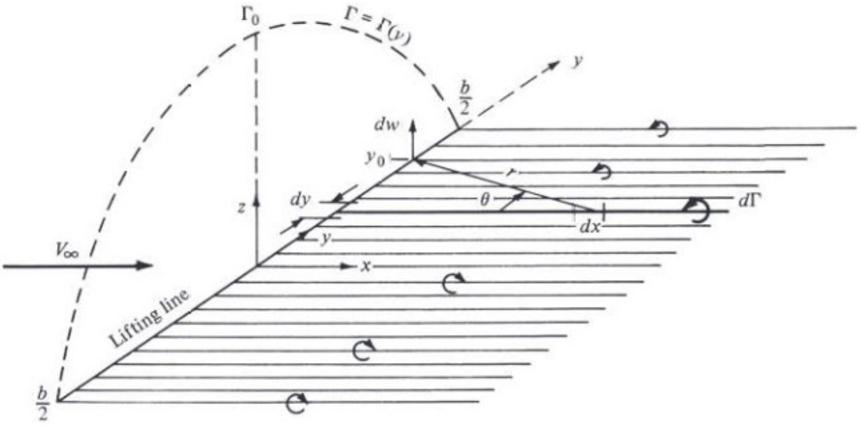
Γ0
Γ = Γ(y)
y
b/2
dw
y0
r
θ
dΓ
dy
z
dx
y
x
V∞
Lifting line
b/2

Figure 4.2: Infinite number of horseshoe vortices superimposed to form a continuous lifting line [1]

along the lifting line and the trailing vortices become a continuous trailing vortex sheet with vortex strength given by Equation 4.2

$$d\Gamma = (d\Gamma/dy)dy \tag{4.2}$$

The magnitude of the total velocity induced by the entire semi-infinite trailing vortex sheet on a spanwise point y_0 is given by Equation 4.3.

$$w\left(y_0\right) = -\frac{1}{4\pi}\int_{-b/2}^{b/2}\frac{(d\Gamma/dy)dy}{y_0 - y} \tag{4.3}$$

4.2.2. VORTEX LATTICE METHODS

The Lifting Line Model is accurate for wings with high aspect ratios, unswept shapes, and subsonic flows. However, predicting the aerodynamic features of highly swept wings requires a better numerical method.

The Vortex Lattice Method divides the wing into multiple elementary wings, which are placed on the mean camber surface of the wing. These lattices are distributed in both chordwise and spanwise directions, as illustrated in Figure 4.3. Each of these elementary lifting surfaces is modeled using a horseshoe vortex, and the bound vortex is placed at the quarter-chord location of the wings. After this discretization process, the Biot-Savart law is used to calculate the velocity induced at the control point of each element by all the elementary wings. Then, the flow tangency condition is applied at the three-quarter chord location of each elementary wing, which provides a set of linear algebraic equations in the unknown vortex circulation strength of each element [16]. This method is computationally efficient, and it allows the modeling of relatively complex geometries, including non-planar surfaces [17].

In a study conducted by Margason, lift coefficients obtained for a 45° swept back wing using the vortex lattice method (VLM), source panel method, and a surface potential distribution method were compared. The results of this comparison are presented in Figure 4.4. As stated by Margason, the vortex lattice method produces results that closely match experimental data due to its ability to disregard the effects of both viscosity and surface thickness. Typically, the impacts of viscosity are counteracted by the effects of surface thickness in most cases.

4.2.3. VORTEX PANEL METHODS

Vortex panel methods are an advancement of the vortex lattice methods that incorporate the thickness of the wing surface. With this approach, the singularities are distributed across the entire wing surface, rather than solely on the mean chord surface. While the accuracy of the numerical results obtained from the vortex panel methods is similar to that of the vortex lattice method (discussed in subsection 4.2.2), the panel methods are considerably more computationally expensive. Additionally, the discrete nature of the singularities still poses a numerical issue with the panel methods, as highlighted by Bramesfeld [18].

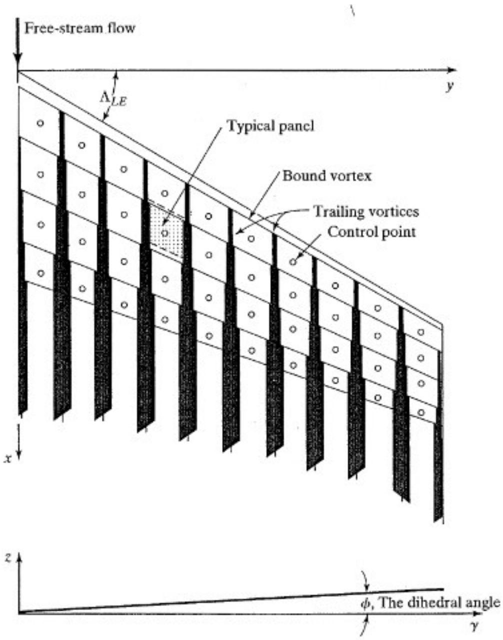
Free-stream flow
y
Λ_{LE}
Typical panel
Bound vortex
Trailing vortices
Control point
x
z
ϕ, The dihedral angle
y

Figure 4.3: Discretisation of lifting surface into elementary wings in VLM ([16])

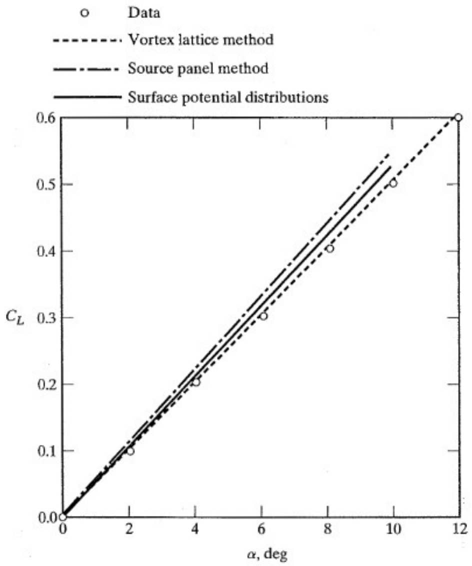

Figure 4.4: Comparison of C_L as a function of AoA for a NACA64A010 section with $AR = 3.0$, $\lambda = 0.5$, $\Lambda_{c/4} = 45°$ [16]

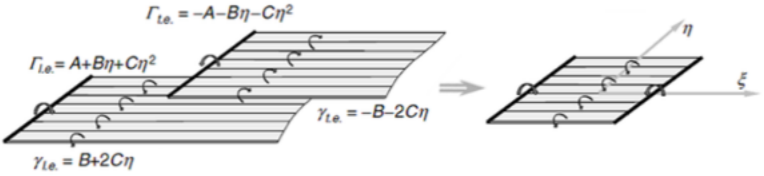
$\Gamma_{t.e.} = -A-B\eta-C\eta^2$
$\Gamma_{l.e.} = A+B\eta+C\eta^2$
$\gamma_{t.e.} = -B-2C\eta$
$\gamma_{l.e.} = B+2C\eta$
η
ξ

Figure 4.5: Composition of DVEs ([17])

4.2.4. HIGHER ORDER METHODS

The previously mentioned methods employ discrete vortex elements to represent the lifting surfaces and the wake in their modeling approach. However, it's important to note that the discrete nature of these elements can introduce numerical instabilities and pose various challenges. These issues become particularly pronounced when dealing with force-free wakes that are permitted to deform.

One of the key problems arises when vortex elements interact with one another or come into close proximity. Under such circumstances, the velocity induced by one element on the other tends to approach infinity. This phenomenon becomes especially problematic when higher panel densities are employed within a force-free wake system, as pointed out by [8].

[18] offers a potential solution to the above-mentioned problem by introducing the concept of distributed vorticity elements. A distributed vorticity element comprises vortex filaments situated along both its leading and trailing edges. These two filaments exhibit spanwise circulation patterns that are parabolic in nature and possess opposite orientations. A sheet with linear spanwise vorticity distribution connects the two vortex filaments, satisfying Helmholtz vortex theorem [18]. The distribution of circulation along the leading and trailing edges is represented by Equation 4.4. The strength of the vortex sheet for the semi-infinite trailing vortex sheet can be calculated using Equation 4.5. To compute the induced velocities resulting from these potential flow elements, it's necessary to consider the contributions from all four elements comprising the DVE: the leading edge filament, the trailing edge filament, the leading edge vortex sheet, and the trailing edge vortex sheet [19], as illustrated in Figure 4.5

$$\Gamma(\eta) = A + B\eta + C\eta^2 \tag{4.4}$$

$$\gamma(\eta) = \frac{\partial\Gamma(\eta)}{\partial\eta} = B + 2C\eta \tag{4.5}$$

The coefficients A, B, and C in Equation 4.4 and Equation 4.5 are determined by applying three boundary conditions. These conditions ensure the enforcement of flow tangency at the control points, continuity of circulation, and continuity of vorticity at the interfaces of two adjacent vortex elements, as detailed in [17].

The velocity induced at an arbitrary location $P_0(\xi_0, \eta_0, \zeta_0)$ by a DVE can be determined by superimposing the velocities induced at that location by the two vortex elements and the streamwise vortex sheet, as described by Bramesfeld [18]. The velocity induced by the two vortex filaments and the semi-infinite vortex sheet is calculated using equations Equation 4.6 and Equation 4.7, respectively.

$$\mathbf{w}_1(\xi_0, \eta_0, \zeta_0) = \int_{-\eta_i}^{\eta_i} \frac{A + \eta B + \eta^2 C}{4\pi r_1^3} \begin{bmatrix} -\zeta_0 \\ \zeta_0 \tan(\varphi) \\ \zeta_0 - \eta_0 \tan(\varphi) \end{bmatrix} \mathrm{d}\eta \tag{4.6}$$

$$\mathbf{w}_2(\xi_0, \eta_0, \zeta_0) = \int_{-\eta_i}^{\eta_i} \frac{B + 2\eta C}{4\pi\left((\eta_0 - \eta)^2 + \zeta_0^2\right)^2} \left(\frac{\zeta_0 - \eta \tan(\varphi)}{r_1} + 1\right) \begin{bmatrix} 0 \\ -\zeta_0 \\ \eta_0 - \eta \end{bmatrix} \mathrm{d}\eta \tag{4.7}$$

$$r_1 = \sqrt{(\xi_0 - \eta \tan(\varphi))^2 + (\eta_0 - \eta)^2 + \zeta_0^2} \tag{4.8}$$

In equations Equation 4.6 and Equation 4.7, the variables ξ, η, and ζ represent the coordinate axes of the local coordinate system associated with the DVE. In this context, η and ξ define the spanwise and chordwise axes, respectively. The local coordinate system is completed by ζ, which specifies the direction normal to the plane of the DVE, following a right-handed coordinate system convention.

Furthermore, ϕ is used to denote the leading edge sweep angle of the DVE relative to the local spanwise axis, η. Additionally, the value of r_1 can be determined using Equation 4.8. The method was validated against results of other theoretical approaches [20, 21, 22]. The research findings have led to the conclusion that the utilization of Distributed Vorticity Elements (DVEs) represents a computationally more efficient approach. This is primarily because it requires a reduced number of spanwise elements while still maintaining a comparable level of accuracy when compared to other relaxed-wake methods. Owing to the method's accuracy, speed, and robustness, the method is well suited for cases where the aerodynamics of the body is strongly influenced by its wake [18]. Since Bramesfeld [18] concluded that the HOFW method developed which uses DVEs was well suited for studying systems in which the wake had a significant influence on the aerodynamics of the system, Cole el al. [23] adapted this method for propeller-wing systems, where the wake of the propeller has a strong influence on the aerodynamics of the wing, and vice versa.

Methodology of HOFW method introduced by Cole et al. [23] for propeller wing interactions: The method developed by Cole et al. [23] employs surface Discrete Vortex Elements (SDVEs) to represent both the propeller and the wing. This approach can be broken down into two primary phases: the initialization step and the time looping step.

During the initialization step, the researchers define the geometries and operating conditions within a global reference frame. In this phase, they also establish the coordinates of the DVE reference frames. Subsequently, the process transitions into the time-stepping loop [23].

Within the time-stepping loop, the propeller and other bodies, whose motion is determined by specified operating conditions, are displaced within the global coordinate system. The key step in solving the problem involves determining the circulation distribution over each SDVE at each time step, as described in Cole et al.'s work [23]. This is accomplished by solving for three coefficients denoted as A, B, and C in Equation 4.4 and Equation 4.5, which characterize the circulation strength of each DVE. The solution for these three coordinates is obtained by applying three boundary conditions as elaborated upon in [17]:

1. Flow tangency condition at the control point of each DVE to ensure that the flow is aligned with the surface.
2. Continuity of circulation at the interface of two DVEs.
3. Continuity of vorticity at the interface of two DVEs.

The wake for each lifting surface is generated using a time-stepping method, allowing for an unsteady analysis of propeller-wake interaction. This approach is also computationally more efficient compared to spatial relaxation methods, as noted by Cole [23]. At each time step, a spanwise row of Discrete Vortex Elements (DVEs) is released, effectively bridging the gap between the lifting surface and the wake released during the previous time step [23].

To calculate the wake-induced velocities, a quasi-steady approach is adopted. This means that the effect of the wake is computed continuously throughout the wake at each time step, without considering a lag. Once the flowfield is computed, the forces acting on each SDVE are determined using the Kutta-Joukowski theorem.

Furthermore, Cole argues that this approach, which models the wake as continuous rather than discrete, results in a more realistic computed velocity field when compared to traditional lower-order methods used to represent lifting surfaces and their wakes. This difference is depicted in Figure 4.6, which illustrates a comparison of velocities induced by a fixed wake in the far field using a traditional lower-order Vortex Lattice Method (VLM) versus the method employing DVEs.

4.3. PROPELLER-WING INTERACTION MODELING TECHNIQUES

The analysis of propeller-wing interactions can be categorized into two main approaches based on the nature of how these interactions are modeled: Full Interaction Mode (FIM) and Single Interaction Mode (SIM). In practice, there exists a mutual influence between the propeller and the wing, where the propeller's slipstream impacts the wing's aerodynamics, and vice versa, as noted in a previous study [24]. To comprehensively understand and analyze the propeller-wing combination, it is imperative to undertake a Full Interaction Mode (FIM) approach [4].

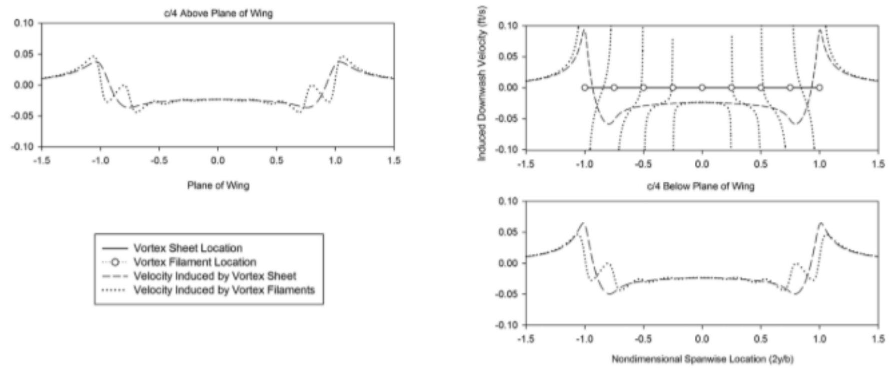

Figure 4.6: Comparison of the induced velocities by a fixed wake at the far field, as modeled by a lower order VLM vs using DVEs ([23])

In their respective research, Witkowski [25] and Veldhuis [7] employ a vortex lattice method (VLM) to simulate and model the propeller-wing system. Notably, both studies utilize a fixed-wake VLM model. However, their approaches differ in how they model the propeller and wing interactions. Veldhuis adopts a two-model approach, employing a VLM model to represent the wing and a Blade Element Momentum (BEM) model to simulate the propeller. In this method, Veldhuis iterates between these two components independently, incorporating the induced velocities calculated for one component into the other, and repeating this process until convergence is achieved. In contrast, Witkowski takes a unified approach by modeling both the propeller and the wing within a single potential field. Moreover, it's noteworthy that both studies incorporate viscous effects using a strip theory, demonstrating their comprehensive analysis of propeller-wing interactions.

As previously outlined in the discussion within subsection 4.2.2, it is important to note that while Vortex Lattice Method (VLM) serves as a valuable tool for assessing propeller-wing performance, it has inherent limitations related to both accuracy and numerical stability. Specifically, traditional VLMs rely on discrete vortex elements, and a potential issue arises when the vortex filaments' centers, where the self-induced velocity tends to approach infinity, are in proximity to the control points of other vortex elements [26]. This situation can potentially introduce numerical instability into the calculations.

Another important aspect of classifying different propeller-wing interaction modeling techniques is the consideration of whether the wake is allowed to deform or not. This classification results in two categories: fixed wake and relaxed wake methods. The aerodynamics of the propeller-wing system are significantly influenced when the wake of the propeller deforms due to the presence of the wing's wake, and vice versa. Notably, the slipstream generated by the propeller undergoes deformation when it interacts with the downstream surface, such as the wing. These effects cannot be accurately captured using a fixed wake model [23]. Therefore, it becomes imperative to employ a free wake model to ensure a comprehensive and accurate analysis of the propeller-wing system.

Several relaxed wake methods have been developed to account for wake deformation. Notably, software tools like VSAero [27] and CAMRAD II [28, 29] permit the advection of control points in response to local flow conditions, including the incorporation of induced velocities added to the freestream. Nevertheless, it's essential to acknowledge that even these advanced methods remain susceptible to numerical instabilities because of the discrete nature of the vortex elements used in their calculations. Additionally, Maretta [30] employed a free wake model in their research, utilizing the lifting line model to represent both the wing and the propeller. However, the accuracy of their findings could not be conclusively assessed since they did not validate their results against experimental or Computational Fluid Dynamics (CFD) data.

The allowance for wake deformation in free wake methods can pose numerical challenges when combined with traditional vortex lattice methods relying on discrete vortex elements. To mitigate this issue in the context of propeller-wing interactions, various studies advocate the use of Distributed Vorticity Elements (DVEs). Bramesfeld ([18]) introduced DVEs as an approach suitable for systems where individual component performance is notably influenced by their own wakes and those of other components within the system. This concept represents an advancement in accurately accounting for complex wake interactions. Moreover, Cole et al. ([31]) validated a higher-order free wake method that incorporates DVEs to model propeller-wing interactions, effectively enhancing accuracy and robustness by addressing the challenges associated with wake deformation.

4.4. MODELING VISCOUS EFFECTS (CORRECTIONS)

While potential flow methods are commonly employed in the study of propeller-wing interactions, they typically neglect the influence of viscous effects. Nevertheless, it's important to recognize that viscous effects do play a role in this phenomenon, contributing to the overall viscosity of the system. Notably, effects such as separation can impact the spanwise lift distribution across the lifting surface, subsequently affecting the induced drag of the system.

To account for these viscous effects in simulations of propeller-wing systems, various approaches have been explored in the literature. For instance, Willemsen [32] utilized a viscous correction method developed by Horsten and Veldhuis [33] to investigate propeller-wing interactions. In this method, an angle of attack correction is applied based on the discrepancy between viscous and inviscid lift.

Cole et al. [31] employed lookup tables to incorporate viscous effects into their analysis. However, it's important to note that this approach may become less accurate when dealing with significant flow separation.

Many other studies acknowledge the significance of including viscous effects in their investigations but may not fully integrate these effects into their studies. Nonetheless, recognizing the importance of viscous effects in propeller-wing interactions is a crucial step toward developing more comprehensive and accurate models for such systems.

5

RESEARCH OUTLOOK

From the literature, it was found that the presence of a propeller has several aerodynamic consequences on the performance of the wing. Thus, it is essential to take into account these interactive phenomena in order to optimize propeller-wing configurations.

5.1. GAPS IN LITERATURE

From the existing literature, it is known that Propeller-based propulsion technology is widely acknowledged for its superior efficiency compared to jet engines. This is primarily attributed to its capability to generate thrust through a marginal increase in the momentum of a substantial volume of air. Furthermore, the close integration between the propulsion system and the airframe offers the potential for enhancing the efficiency of the propulsion-airframe system. In the pursuit of this objective, numerous studies exist, which explore various propeller wing configurations, encompassing aspects such as relative propeller location, relative propeller size, propeller rotation direction, propeller loading, wing loading, and more. However, a thorough examination of the literature reveals the presence of certain less evident gaps that require attention.

- Currently, there is limited available literature investigating the propeller-wing interaction phenomenon specifically for distributed propulsion configurations.

- In the field of propeller-wing interaction studies for leading-edge distributed systems, there exists a noticeable gap in research focusing on the upstream influence of the wing on the propeller. The majority of studies tend to focus on the downstream effects and often overlook the interactive benefits on the propeller itself. However, it is crucial to assess the upstream influence as well in order to obtain a comprehensive understanding of the overall improvement in system performance.

5.2. RESEARCH QUESTIONS

These research gaps naturally give rise to the following main research question which can be split into smaller sub-research questions:

"How does the implementation of multiple leading-edge distributed propellers influence the system's performance, and in what ways do the interactive advantages differ from those observed in a single propeller-wing system?"

This main research question can be split into the following sub-research questions:

- "What constitutes the most appropriate metric for evaluating and comparing two propeller wing systems, and based on this metric, how does the performance of a leading-edge distributed propeller system compare with that of a single propeller system?"
- "How does the integration of tractor propellers in a leading-edge distributed propeller system affect the induced drag of the wing, and how does this effect compare to the influence of a single propeller system on the induced drag of the wing?"
- "How does the integration of tractor propellers in a leading-edge distributed propeller system influence the efficiency of the propellers, η_p, in comparison to the effect of a single propeller system on the same efficiency metric, η_p"

6

METHODOLOGY

This chapter of the thesis outlines the methodologies used in the study, including various computational tools and techniques. section 6.1, discusses the creation and meshing of geometries for wings and propellers using the FlightStream software. This is followed by section 6.2, where the implementation of an unsteady relaxed wake panel method is detailed to examine propeller-wing interactions. subsection 6.2.1 deals with the vortex panel method, pivotal in understanding the solver. subsection 6.2.2 addresses the integration of boundary layer methods for including viscosity effects. The chapter then addresses the methods available in FlightStream for calculating forces and moments on bodies in subsection 6.2.3.

6.1. GEOMETRY AND MESH GENERATION

This section outlines the procedures for creating and meshing the geometries of interest, specifically the wing and propeller. The process employed the Component Cross Section (CCS) file format, which facilitates the automatic meshing of geometries in FlightStream. The 3-D cross-sections of each geometry component are delineated and saved in an ASCII text file. A key aspect of FlightStream's design methodology is the assignment of a specific type to each geometry component. This categorization allows the software to generate surface meshes automatically, with each mesh being specifically tailored to the distinct features of the individual component [34]. The cross-sections that were used to define the geometries of the wing and propeller are illustrated in Figure 6.1. An instance of the generated wing and propeller meshes using the CCS file format in FlightStream is presented in Figure 6.2.

6.2. AERODYNAMIC ANALYSIS

The next step after geometry creation and mesh generation is choosing an appropriate solver to set up and perform the calculations. For this purpose, a panel method was chosen to provide the right balance between fidelity and computational cost. However, to fully answer all the research questions, it is necessary to use an unsteady relaxed wake

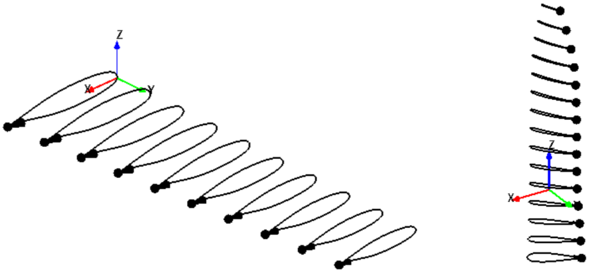

(a) Wing cross sections for mesh generation

(b) Propeller cross sections for mesh generation

Figure 6.1: Wing and propeller cross sections used for generating surface mesh using the CCS method

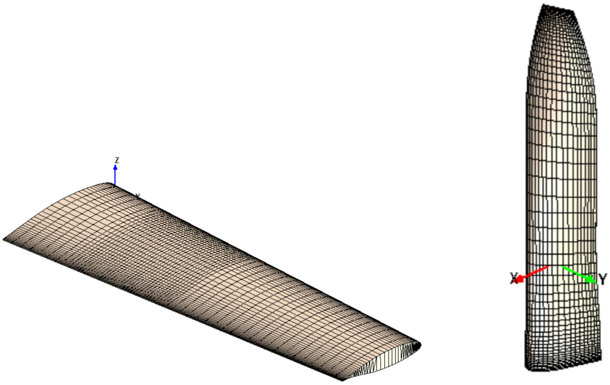

(a) Sample wing mesh

(b) Sample propeller mesh

Figure 6.2: Sample surface meshes generated using the CCS method

panel method to fully capture the two-way interaction between the propeller and the wing. Both the wing (with its wake) and the propeller (with its wake) need to be modeled using unsteady panel methods as one of the aims of this research is to quantify the impact of the propeller-wing interaction on the propeller performance. This cannot be achieved by using an actuator disc model to model the propeller. A detailed description of the panel method and the way it is implemented in FlightStream is given in subsection 6.2.1.

6.2.1. PANEL METHODS

The vortex panel method, a central aspect in FlightStream software, provides a more efficient approach to simulating aerodynamic flows. Rooted in the concept of potential flows, these methods simplify flows by treating them as irrotational and incompressible. By employing singularity elements such as potential vortices, doublets, and sources, the potential flow techniques effectively represent the flow field with a singular variable: the velocity potential, ϕ [17]. However, it is important to note that these models are most effective in scenarios where viscous effects, including flow separation, are minimal.

One of the key strengths of potential-flow solutions is their linearity, which allows for the straightforward superposition of effects to model complex flow scenarios. In vortex panel methods, the lifting surface is segmented into multiple elementary wings, both spanwise and chordwise. This approach not only models the curvature but also the thickness of the lifting surfaces. Each elementary wing is modeled using vortex elements. These vortex elements collectively contribute to the velocity field, superimposing upon the freestream. The strength of each vortex element is determined by enforcing the tangential flow boundary condition at the control point of each panel. Subsequently, the complete velocity field can be deduced from the vortex strengths, and the pressure field is derived from the velocity field.

It is fortunate that, in most flow conditions, the rotational flow is predominantly confined to a small region within the boundary layer [35]. The advantage of using panel methods is that the entire flow field does not require discretization. It is sufficient to generate a surface mesh instead of meshing the whole volume, leading to a more manageable system of linear equations to be solved.

The unsteady panel method in FlightStream allows for a time evolving development of the wake, which enables the study of two way interaction between the wing and the propeller. This is essential to accurately simulate the propeller-wing interaction in a full interaction mode (FIM). FIM is crucial for capturing the effects of the propeller on the wing aerodynamics, as well as the reciprocal influence of wing aerodynamics on the propeller. Moreover, using a fully unsteady approach allows for a force-free description of the wake, which captures interaction effects that are a result of the deformation of the propeller and wing wakes due to each other. This approach to simulating propeller-wing interactions, employing an unsteady vortex panel method, has been successfully executed and validated for accuracy in studies conducted by Ahuja and Litherland [36].

RELAXED WAKE METHOD

Some of the causes of the interaction between the propeller and the wing is a result of the deformation of their respective wakes due to each other [23]. This effect can only be captured using a fully unsteady relaxed wake method, which is a key feature in the unsteady solver in FlightStream. FlightStream implements the relaxed wake method using a time evolving technique. In this method, the lifting surface is advanced in each time step. As it progresses, a new array of panels, carrying vorticity, is released to bridge the gap between the trailing edge of the lifting surface and the array of wake panels released in the previous time step. The wake panels are allowed to translate and rotate and stretch according to the local velocity at each time step (see Figure 6.3). This velocity is a superposition of the induced velocities due to all potential elements present in the previous time step and the freestream velocity. This allows for a force-free description of the wake.

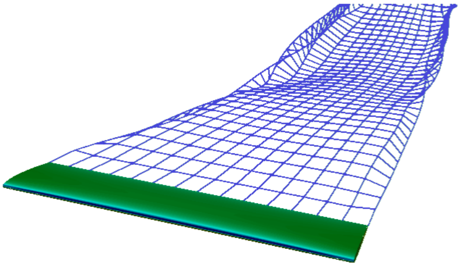

Figure 6.3: Relaxed wake of a wing [37]

6.2.2. VISCOUS COUPLING

Viscous coupling in FlightStream is carried out using the boundary layer method. The boundary layer method is used to couple viscous effects with a potential flow method such as panel methods. The boundary layer can be integrated into a potential flow solution to include the effects of viscosity. Essentially, the potential flow is modified based on the displacement thickness of the boundary layer, which is determined by the velocity distribution at the edge of the boundary layer [38]. A short overview of how the boundary layer method is coupled with the 3-D panel method used in FlightStream is provided here. The detailed description is given in [39]. The aerodynamic solution is iteratively modified to take boundary layer effects into account. The panel method ignores the boundary layer in its first prediction of the potential flow field. Based on this flow field, the boundary layer approach then computes the boundary layer properties. These properties in turn alter the panel method's boundary conditions for the next iteration. Until the solution converges and offers a more realistic depiction of the aerodynamic behavior, this iterative cycle is continued. This process is depicted in Figure 6.4

FlightStream software provides three ways to model the boundary layer - laminar, tur-

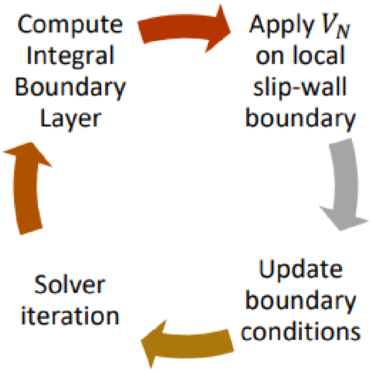
Compute Integral Boundary Layer
Apply V_N on local slip-wall boundary
Update boundary conditions
Solver iteration

Figure 6.4: iterative process for viscous coupling in FlightStream [39]

bulent, and transitional turbulent boundary layer.

1. Laminar Boundary Layer: This method assumes smooth, laminar flow. Typically, it is used in cases where the flow is predicted to fall in the low Reynolds number regime where the fluid movement is orderly and the layers are expected to slide past each other. In this model, the boundary layer is modeled using the Thwaites method [40].

2. Turbulent Boundary Layer: This method is used for flows where the flow is predicted to fall in the high Reynolds number regime, and the fluid motion is expected to be highly irregular, with eddies. Increased energy dissipation and momentum transfer are expected in the boundary layer. FlightStream uses a modified version of the method developed by Standen [41] to develop this boundary layer on top of the potential flow solution.

3. Transition Boundary Layer: This method is suitable for cases where the flow is expected to fall between the laminar and turbulent states. The boundary layer type is changed at the transition point predicted using the method developed by Dvorak et al. [42]

6.2.3. FORCES AND MOMENTS

In FlightStream, there are two methods available to determine the forces and moments acting on a body. These methods are based on surface pressure integration and vorticity calculations. The vorticity method relies on the Kutta-Joukowski theorem, while the surface pressure integration method utilizes pressure distribution along a contour and numerical integration techniques. However, it's worth noting that the studies conducted by Smith et al. [43] and Towne et al. [44] have demonstrated that the surface pressure integration technique is highly sensitive to the panel densities in both the chordwise and spanwise directions. To obtain accurate force and moment values through surface integration, exceptionally high panel densities are required in both directions.

As a result of these findings, the vortex method has been chosen as the preferred approach for calculating forces and moments in FlightStream. For instance, the lift force at a specific spanwise station on a lifting surface (L_y) is determined using the Kutta-Joukowski theorem, where the circulation around the local airfoil section at that spanwise station (Γ_y) plays a crucial role, as described in Equation 6.1. Similarly, the induced drag force at a local spanwise station is computed by calculating the downwash at that station (w_y), as illustrated in Equation 6.2, and then using this information to calculate the induced drag at the same spanwise station, as shown in Equation 6.3. However, it's important to note that the drag force calculated by this method is the induced drag calculated after the iterative boundary layer development process described in subsection 6.2.2. Nonetheless, even though the viscous boundary layer is included in this calculation, the drag obtained through Equation 6.3 represents solely the induced drag component of the total drag. The skin friction drag is obtained using analytical equations depending on the boundary layer properties computed using boundary layer model. It is important to note that when the propeller is involved, the induced upwash due to all the wake panels (propeller and wing wake) are included in the induced drag calculation in Equation 6.3. It is validated in the next chapter that the propeller velocities are included in the induced drag calculations. In Equation 6.2, $w_{y,p}$ denotes the downwash induced on the wing at a spanwise station resulting from the propeller surface and wake vortex elements.

$$L_y = \rho_\infty V_\infty \Gamma_y \tag{6.1}$$

$$w_y = \frac{1}{4\pi}\int_{-\frac{b}{2}}^{\frac{b}{2}} \left(\frac{1}{y - y_0}\right) \frac{-d\Gamma_{y_0}}{dy} dy_0 + w_{y,p} \tag{6.2}$$

$$D_{(i,y)} = \rho_\infty w_y \Gamma_y \tag{6.3}$$

7

VALIDATION

This chapter is dedicated to the validation of the FlightStream software, to confirm its computational robustness and accuracy in addressing the research questions at hand. This validation is crucial in ensuring that the software's outputs are reliable. It begins with an initial validation, exploring different methods for evaluating forces and the capabilities of FlightStream. This is followed by a detailed study on wing mesh refinement. The chapter then delves into isolated validations of both the propeller and the wing, before culminating in a comprehensive validation of the combined propeller-wing system.

7.1. INITIAL VALIDATION

In this thesis, the primary objective is to evaluate the performance benefits of leading-edge distributed propeller systems over single propeller systems. In order to predict this correctly, it is essential that the analysis tool is able to predict the effect of propeller swirl on the wing. This is because swirl recovery is an important component of induced drag in propeller-wing interactive systems. Thus, it is essential to look at the various methods available in FlightStream to calculate the lift and drag from the solution.

7.1.1. DIFFERENT METHODS TO EVALUATE FORCES

The FlightStream 3D panel method employs a vorticity distribution across a body surface to analyze and predict its aerodynamic characteristics. Once the vorticity distribution over the surface is obtained through the application of tangential flow boundary conditions, the velocity and pressure distributions can be obtained over the body under analysis.

Once the velocity and pressure distributions are obtained over the surface, FlightStream provides two distinct approaches for calculating lift, moment, and induced drag, as described in subsection 6.2.3. The first method relies on surface pressure integration, while the second is vorticity-based. The vorticity method is grounded in the Kutta-Joukowski theorem, whereas the surface pressure integration method involves analyzing pressure distribution along a contour using numerical integration techniques. It is noteworthy to mention that research conducted by Smith et al. [43] and Towne et al.[44] has underscored the sensitivity of the surface pressure integration technique to panel densities in both the chordwise and spanwise directions.

To choose the appropriate method for calculating forces, a comparative study is conducted initially for an isolated wing. Subsequently, these methods are compared in the context of a simple propeller-wing system.

For this comparative study, simulations were conducted on a simple NACA0012 wing with an aspect ratio of 10, encompassing both viscous and inviscid conditions. Lift and drag distributions were determined using both the Kutta-Joukowski theorem and surface pressure integration techniques. In inviscid scenarios, it is anticipated that the lift and drag distributions obtained through the Kutta-Joukowski method closely resemble those derived from surface pressure integration. This expectation arises from the inherent assumption of inviscid flow in the Kutta-Joukowski theorem, thereby aligning with the predictions of surface pressure integration under inviscid conditions. Conversely, deviations are expected between the two methods for viscous simulations. Additionally, for both viscous and inviscid simulations, overlapping drag distributions are anticipated when employing the Kutta-Joukowski method and surface pressure integration, given that the former relies on the assumption of inviscid flow.

The lift and drag distributions for the NACA0012, aspect ratio 10 wing are depicted in Figure 7.1a and Figure 7.1b. Several significant observations can be drawn from these figures. Firstly, we look at the inviscid lift and drag distributions. It is observed that there is minimal difference between the two methods for the lift distribution, whereas the drag distribution exhibits significant variation. As explained in subsection 6.2.3, the drag calculation obtained from the surface pressure integration method is very sensitive to the paneling density in both chordwise and spanwise directions. The lift calculation, however, is less sensitive to the paneling density.This is attributed to the fact that pressure distribution varies most significantly near the leading edge of the wing, where the surface area perpendicular to the drag direction has the greatest influence. Panels situated behind this leading edge region are predominantly oriented in the lift direction, where the impact of panel density on pressure variation is less pronounced. Thus, there is a large discrepancy in the drag distributions obtained from the two methods. Consequently, the inviscid lift distributions closely match each other and align with the inviscid lift distribution curve obtained from an XFLR5 (Xfoil) analysis. Additionally, the inviscid drag distribution also exhibits good agreement with the curve obtained from XFLR5.

Now, we examine the viscous lift and drag distributions. Once again, due to the same reasons explained for the inviscid comparisons, the viscous lift curves obtained with the Kutta-Joukowski (KJ) method and the surface pressure integration methods overlap, whereas the drag distributions show significant divergence. An interesting observation is that the drag distributions computed by the Kutta-Joukowski method are nearly identical for both the viscous and inviscid simulations. This occurs because the Kutta-Joukowski method provides induced drag distributions for both viscous and inviscid cases. Specifically, it transforms the circulation distribution into an equivalent lifting line along the trailing edge of the wing. This equivalent lifting line allows for the calculation of downwash at each spanwise station using Equation 6.2, which then enables the determination of the total induced drag of the wing using Equation 6.3. Thus, the Kutta-Joukowski method produces the induced drag distribution for both viscous and inviscid simulations. However, the distinction lies in the fact that, for the viscous case, the boundary layer thickness is taken into account when solving for the circulation strengths. Nevertheless, there is minimal difference observed between the viscous KJ and the inviscid KJ drag distributions, mainly due to the very high Reynolds number in the analysis (around 2.8 million). This results in an extremely thin boundary layer, which has minimal impact on induced drag distributions.

To explore this further, a cambered airfoil (NACA2412) is simulated at a 7-degree angle of attack with a lower Reynolds number of approximately 515,000. This was done to accurately capture the effect of boundary layer thickness on lift and drag distributions. Figure 7.2a and Figure 7.2b illustrate the lift and induced drag distributions for both inviscid and viscous coupled cases at the lower Reynolds number of 515,000. Here, a distinct offset can be observed in both lift and drag distributions between the inviscid (black curve) and viscous (red curve) cases. The viscous lift distribution curve clearly falls below the inviscid lift distribution curve. This is because the viscous coupling takes into account the thickness of the boundary layer, which reduces the camber of the wing sections, resulting in lower lift.

It is particularly intriguing to note that the viscous drag curve computed by the Kutta-Joukowski method lies below the inviscid drag curve obtained by the same Kutta-Joukowski method. This phenomenon can be explained by the underlying principles of the Kutta-Joukowski method. The drag calculated by the Kutta-Joukowski method for both viscous and inviscid cases is the induced drag. In the case of viscous coupled simulations, the Kutta-Joukowski method calculates this induced drag based on the circulation distribution, considering the boundary layer thickness. This leads to lower induced downwash velocities for the viscous computations compared to the inviscid computations. Consequently, the induced drag computed with the Kutta-Joukowski method for viscous simulations is lower than that for inviscid simulations.

7.1.2. CAPABILITY OF FLIGHTSTREAM TO ACCOUNT FOR PROPELLER SWIRL VELOCITIES

In this section, FlightStream's ability to capture swirl recovery, a significant factor in the total induced drag of propeller-wing systems, is assessed. To demonstrate the effectiveness of the Kutta-Joukowski method in modeling this phenomenon, a specific test configuration is utilized. This configuration comprises a six-bladed XPROP propeller with a diameter of 1m ($2D_P/b = 0.2$), positioned in front of a symmetric NACA0012 wing with an aspect ratio of 10. The propeller is situated at coordinates $y_P = 0.3(b/2)$, $x_P = 0.4D_P$, and $z_P = 0$, and it operates at an advance ratio of $J = 2.159$. The wing is set at a zero-

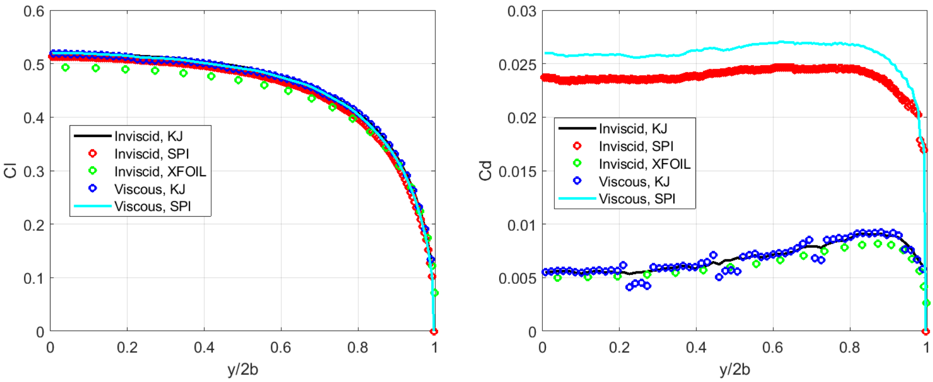

(a) Lift distribution (b) Drag distribution

Figure 7.1: Comparison of different methods to calculate lift and drag distributions over the wingspan of a NACA0012 AR 10 wing at 5 deg AoA, Re = 2.8 Million

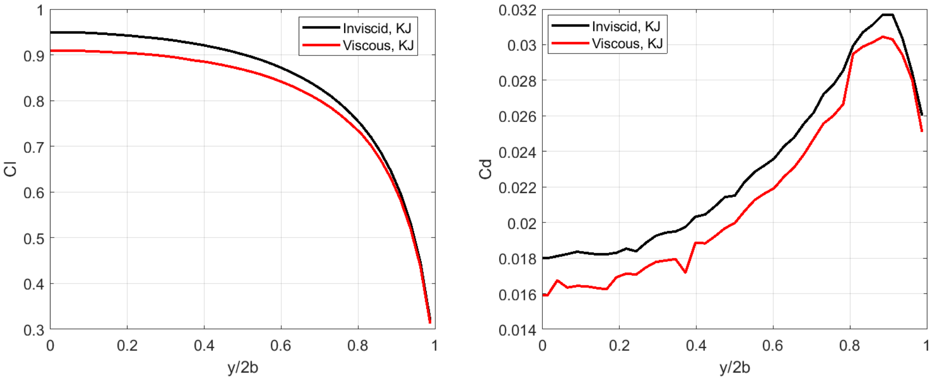

(a) Lift distribution (b) Induce drag distribution

Figure 7.2: Comparison of Kutta-Joukowski method with and without viscous coupling to calculate lift and drag distributions over the wingspan of a NACA2412 AR 10 wing at 7 deg AoA, Re = 515,000

degree angle of attack to isolate the effects of propeller swirl velocities on the induced drag distribution. For a high aspect ratio wing with a symmetric airfoil set at zero angle of attack (AoA), the area of the wing outside the propeller slipstream generates minimal lift, resulting in negligible induced drag, as illustrated by the red line in Figure 7.4a and Figure 7.4b. This allows for the isolation of the propeller slipstream's effect on the wing, as there is minimal lift contribution beyond the slipstream's influence. Assuming the solver and Kutta-Joukowski calculations accurately capture the swirl recovery effect of the propeller, it is anticipated that the propeller slipstream influences the wing by inducing negative induced drag on both sides of the propeller. This occurs because the resultant local lift vector points forward for both the upgoing and downgoing sides of the propeller at zero lift, as depicted in Figure 7.3.

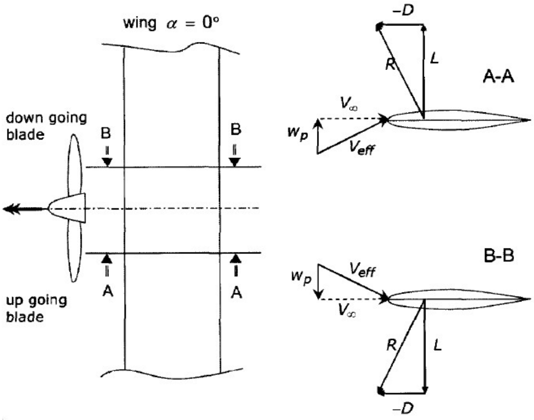

Figure 7.3: Tilting of the resultant force vector on either side of the propeller for a symmetric airfoil wing at $\alpha = 0°$ [7]

Figure 7.4a and Figure 7.4b depict the lift and drag distributions obtained for this test. The lift distribution accurately captures the influence of propeller swirl velocities, exhibiting positive peaks on the upgoing blade side and negative peaks on the downgoing blade side. To further explain the impact of propeller swirl on induced drag distribution (swirl recovery), it's important to note that the induced drag is negative on both the upgoing and downgoing blade sides. This observation confirms that the solver and the Kutta-Joukowski method effectively capture swirl recovery, as explained by Veldhuis [7]. When the wing is set at a zero lift angle of attack, the resultant lift vector is amplified and tilted forward in the upgoing blade region, and is attenuated and tilted forward in the downgoing blade region. The resulting lift gradient implies negative and positive peaks behind the upgoing and downgoing blade sides. The presence of two negative peaks in Figure 7.4b confirms that the solver and the Kutta-Joukowski method accurately account for the swirl recovery effect.

However, it may appear from Figure 7.4b that induced drag outside the propeller slipstream is negligible or zero. This is due to the presence of a very small lift gradient outside the slipstream resulting from the zero lift angle of attack configuration. Therefore, to validate that the Kutta-Joukowski method accurately represents the influence of the circulation distribution on the wing, another simulation was performed with identical parameters, but with a wing angle of attack set at 2 degrees. The lift and drag distributions resulting from this simulation are displayed in Figure 7.5. As seen in Figure 7.5b, there is a non-zero drag distribution outside the propeller slipstream. This verification establishes that the solver and the Kutta-Joukowski method for calculating forces can accurately capture propeller swirl recovery and circulation gradient induced drag.

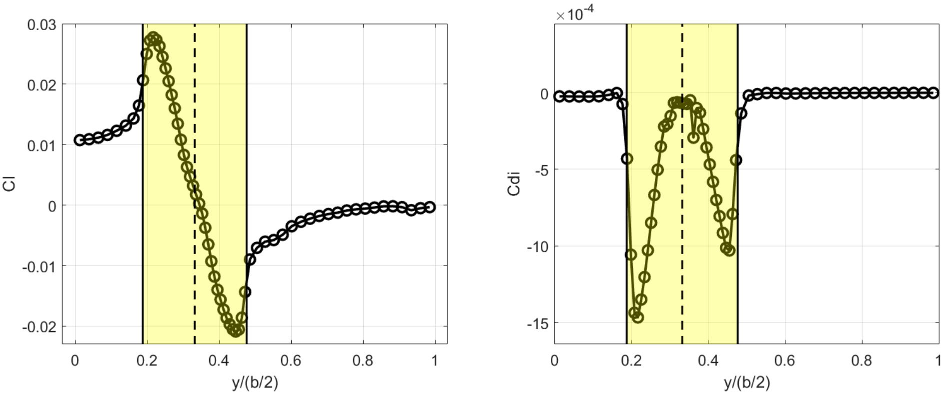

(a) Lift distribution

(b) Induced drag distribution

Figure 7.4: Lift and drag distributions for a simple NACA0012 wing at 0 deg AoA with a leading-edge mounted propeller to ensure that swirl velocities are captured well

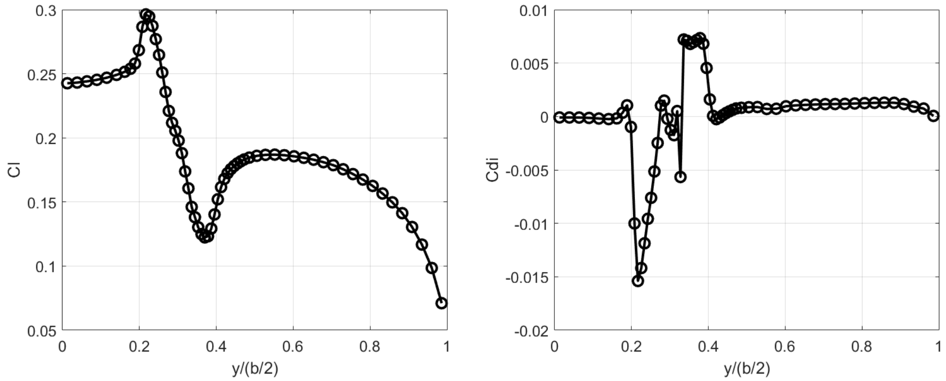

(a) Lift distribution

(b) Induced drag distribution

Figure 7.5: Lift and drag distributions for a simple NACA0012 wing at 2 deg AoA with a leading-edge mounted propeller to ensure that induced drag is not completely 0 outside the slipstream boundaries

7.2. MESH REFINEMENT STUDY

This section deals with the mesh refinement study performed for the wing and the propeller in order to ensure computational efficiency and accuracy.

The geometry of the aircraft wing employed for the mesh refinement study corresponds to that utilized in the research conducted by Della Corte et al. [45]. Their study focused on simulating a wing system equipped with tip-mounted propellers, with specific emphasis on assessing the impact of these propellers operating in energy harvesting conditions on overall wing performance. The experimental campaign included tests involving the wing alone, the uninstalled propeller, the wing with the nacelle installed (no propeller), and the wing with the propeller installed. The geometry of the wind tunnel test model is depicted in Figure 7.6. For this section, the isolated wing geometry, excluding the nacelle or propeller, was employed for the mesh refinement study.

The primary objective behind this mesh refinement study was to ensure that the computational results remained consistent and unaffected by variations in grid size, both in the chordwise and spanwise directions.increased, the mesh refinement for this The study effectively demonstrated the convergence of several essential aerodynamic coefficients. These coefficients included the integrated lift coefficient (CL), the induced drag component (CDi), and the profile drag component (CDo). The convergence of these coefficients with chordwise and spanwise paneling are presented in Figure 7.7 and Figure 7.8 respectively.

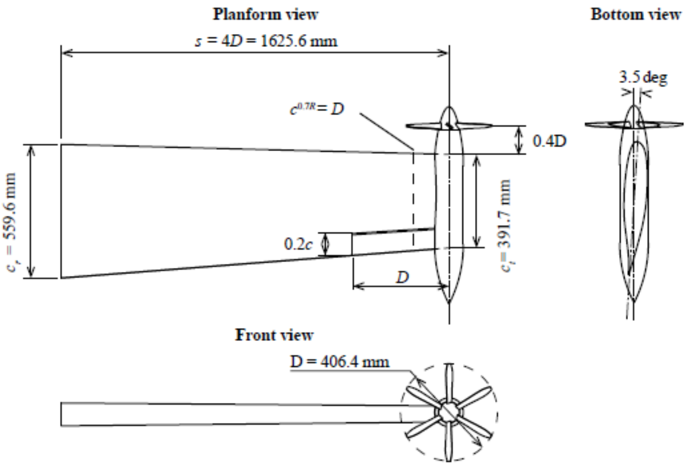

Figure 7.6: Orthographic views of the propeller-wing setup used for validation [46]

7.2.1. CHORDWISE GRID REFINEMENT STUDY

Initially, the number of panels was progressively increased to ensure that the solution did not rely on chordwise paneling. For this study, the number of spanwise panels was fixed at 40. The aerodynamic coefficients (CL), (CDi), and (CDo) were plotted for the successive grid densities in Figure 7.7. In this study, the solution is deemed to have converged if the solution obtained for two successive grids is less than 10%. The aerodynamic coefficients are also listed in Table 7.1.

From Table 7.1 and Figure 7.7, it is evident that the lift and induced drag coefficients converge more quickly than the profile drag coefficient as the chordwise paneling density increases. This can be attributed to the fact that the profile drag is calculated in FlightStream by using the boundary layer properties, which are obtained through an iterative development of the boundary layer over potential flow solutions. Specifically, the first boundary layer is developed over the surface of the wing. Given that the wing exhibits significant curvature near the leading edge, the chordwise paneling in this region needs to be fine enough to accurately capture the profile of the wing section.

The absolute difference between the coarse and fine mesh for the CL, CDi, and CDo are 0.87%, 0.47%, and 5.34%, respectively. In this context, the coarse grid with 120 chordwise panels and the fine grid with 160 chordwise panels are being considered. Consequently, the solution was deemed to be independent of the chordwise paneling density beyond 120 chordwise panels.

N_chordwise	CL	Cdi	Cdo
20	0.4998	0.0164	0.0079
40	0.5895	0.0198	0.0102
60	0.627	0.0209	0.0117
80	0.6296	0.0206	0.0128
100	0.6315	0.0211	0.0131
120	0.6315	0.0211	0.0131
140	0.6414	0.0209	0.0136
160	0.626	0.0212	0.0138
180	0.6254	0.021	0.0139
200	0.6222	0.0211	0.0139

Table 7.1: Chordwise grid convergence

7.2.2. SPANWISE GRID REFINEMENT STUDY

After successfully achieving convergence with respect to chordwise paneling, a grid convergence study was performed to ensure grid convergence with respect to spanwise paneling. For this, the number of chordwise panels was fixed at 120. The convergence of aerodynamic coefficients are plotted in Figure 7.8 and listed in Table 7.2

Evidently, the spanswise grid convergence is much faster with respect to all the aerodynamic coefficients considered. If the grid with 20 spanwise elements is considered the coarse grid and the grid with 40 spanwise elements is considered to be the fine mesh, the absolute difference between the coarse and fine mesh for the CL, CDi, and CDo are 0.22%, 0.95%, and 0.72% respectively.

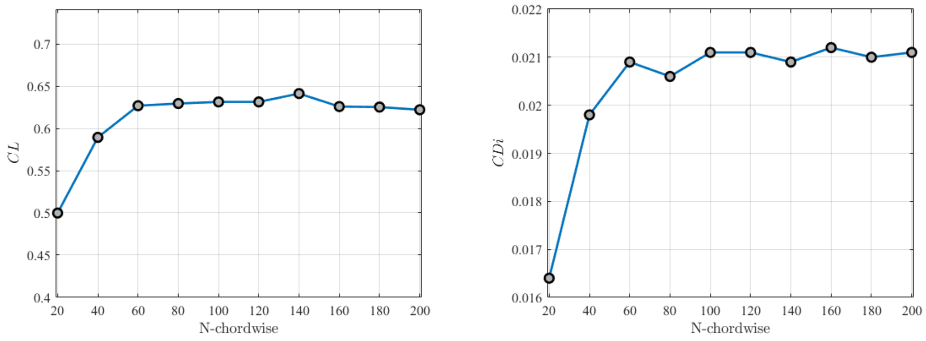

(a) Lift Coefficient

(b) Induced drag coefficient

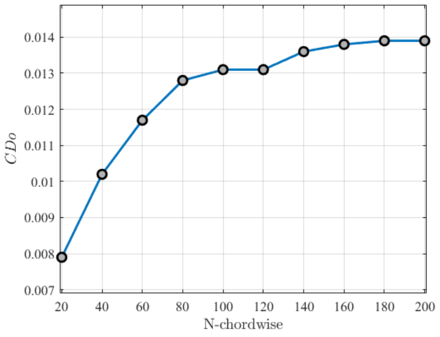

(c) Profile drag coefficient

Figure 7.7: Grid convergence test in the chordwise direction

The convergence of the grid in the spanwise direction is considerably faster than in the chordwise direction because the pressure gradients are significantly smaller in the spanwise direction compared to the chordwise direction. As a result, a greater number of panels, particularly near the leading edge and the trailing edge, are necessary in the chordwise direction to attain grid convergence, as opposed to the spanwise direction.

Analyzing Figure 7.7 and Figure 7.8, it becomes apparent that chordwise refinement significantly influences the computation of viscous drag or zero lift drag (CDo) in comparison to lift (CL) and inviscid drag (CDi). Conversely, spanwise refinement has a more pronounced impact on induced drag (CDi) and the integrated lift coefficient (CL) since these aspects are more reliant on the spanwise distribution of lift. This observation aligns with the intuitive understanding that the shape and curvature of the airfoil are of greater importance in predicting viscous drag and the development of the boundary layer.

N_span	CL	CDi	CDo
10	0.6554	0.0217	0.0129
20	0.6207	0.0213	0.0138
30	0.6232	0.0211	0.0137
40	0.6221	0.0211	0.0139
60	0.6254	0.0213	0.0138
80	0.6258	0.0212	0.0138
100	0.6262	0.0212	0.0139

Table 7.2: Spanwise grid convergence

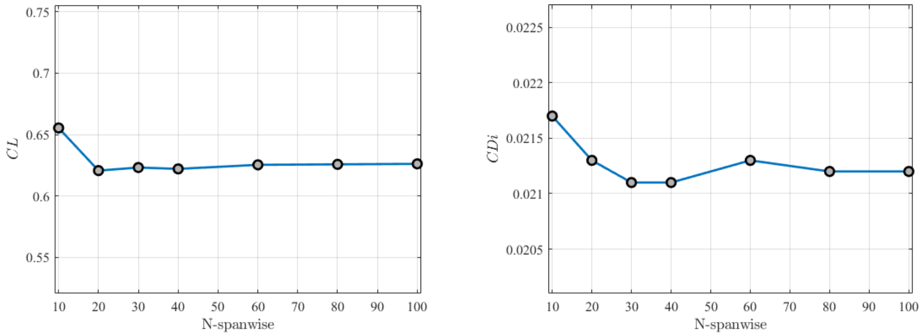

(a) Lift Coefficient

(b) Induced drag coefficient

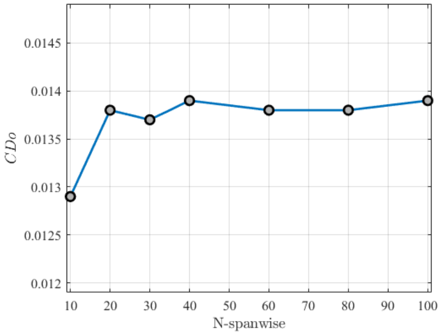

(c) Profile drag coefficient

Figure 7.8: Grid convergence test in the spanwise direction

Hence, the wing was meshed with 120 chordwise panels and 40 spanwise panels. A similar grid convergence study was conducted on the propeller, resulting in a converged solution obtained with 100 chordwise panels and 30 spanwise panels.

7.3. ISOLATED PROPELLER

The validation of FlightStream's capability to predict isolated propeller performance was conducted using experimental data provided by Della Corte et al.[46]. These experiments took place in the TU Delft low turbulence tunnel (LTT), which is a low-speed, closed-circuit wind tunnel characterized by an octagonal cross-section. Throughout the tests, a turbulence level lower than 0.1% was maintained.

The propeller model examined in these experiments was the six-bladed TUD-XPROP propeller, featuring a diameter of 0.4064m. The pitch angle of the blades was defined at $r/R = 0.7$. For the purpose of validation, data corresponding to two different pitch angles, namely $\beta_{0.7} = 30°$ and $\beta_{0.7} = 45°$, were employed. Additionally, the radial distribution of chord and pitch angle for $\beta_{0.7} = 20°$ is illustrated in Figure 7.9a.

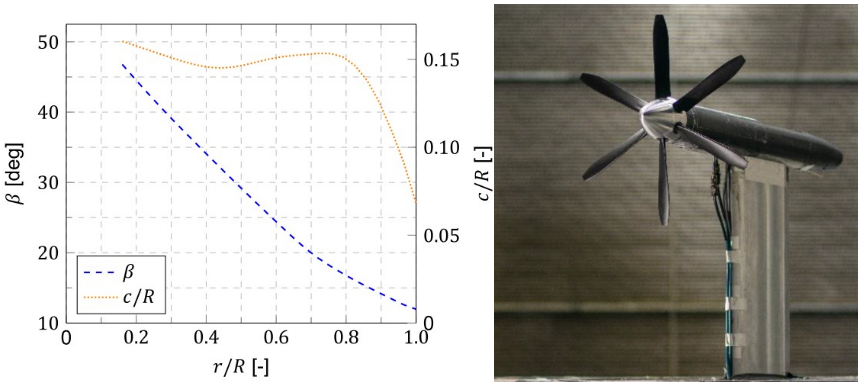

(a) Twist and chord distribution of the TUD-XPROP propeller [32]

(b) Wind tunnel model of the TUD-XPROP propeller [47, 48]

Figure 7.9: TUD-XPROP propeller

Two methods for modeling the propeller in FlightStream exist. The first method models the entire blade, including the blade's thickness. In this approach, both the pressure and suction sides are meshed and modeled with vortex elements. The second method models only the mean camber surface of the blade without considering the thickness. In this approach, the VLM is used instead of VPM. Figure 7.10a compares the performance parameters C_T (Figure 7.10a), T_C (Figure 7.10b), C_P (Figure 7.10c), and η_P (Figure 7.10d) predicted by the FlightStream solver using a mean surface approximation of the blade and using the full blade. The experimental values are plotted against these predicted values in the figure. The performance parameters for both methods are listed in Table 7.3 and compared against the experimental results. The definitions of these propeller performance parameters are provided in Equation 2.3, Equation 2.4, Equation 2.5, and Equation 2.2 respectively.

In Table 7.3, errors concerning the numerical methods with respect to experimental tests are provided within brackets. It is apparent that both the mean surface method and the

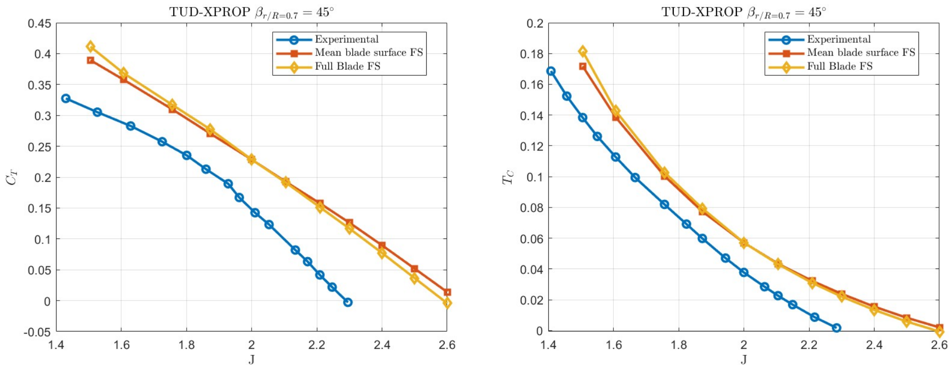

(a) C_T (b) T_C

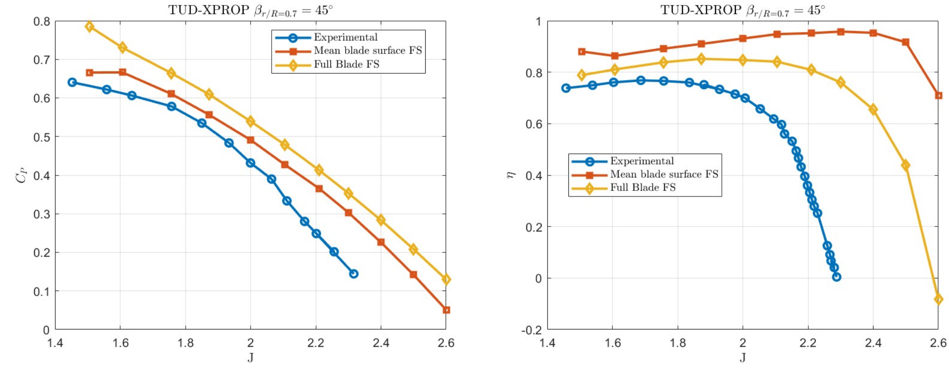

(c) C_P (d) η

Figure 7.10: Validation of isolated propeller performance prediction

Performance parameter	Full blade simulation	Mean surface approach	Experiment
C_T	0.277 (30%)	0.270 (25.3%)	0.212
C_P	0.609 (14%)	0.556(4.12%)	0.534
T_C	0.079 (31.66%)	0.077 (28.33%)	0.060
η_P	0.86 (14.66%)	0.91(21.33%)	0.75

Table 7.3: Performance parameters for isolated propeller

full blade simulation yield similar errors in predicting C_T and T_C compared to the experimental results. Both methods tend to overpredict C_T and T_C by approximately 30%. However, in the case of C_P, the mean surface approach exhibits a 4.12% error, whereas the full blade method shows a 14% error. This suggests that the mean surface method significantly underestimates torque. Consequently, there is a considerable error in efficiency for the mean surface approach (21.33%), compared to the 14.66% error obtained with the full blade simulation. Given that the error obtained using the full blade simulation exhibits a consistent trend across all performance parameters, it is deemed much more reliable than the mean surface method. Furthermore, considering the significance of the interaction effect on the propulsive efficiency of the propeller in this study, the decision was made to employ the full blade simulation for the unsteady simulation of the propeller. The high error is likely to be a combination of modeling error and uncertainty in the wind tunnel experiments from which the experimental plots are extracted.

7.4. ISOLATED WING

Validating the solver's capability to predict wing performance, important to ensure that the solver is capable to be used to anser the research questions posted earlier. To accomplish this, the selected wing was sourced from the work of Della Corte et al., which was a part of the FUTPRINT50 project [45]. This wing model is characterized by a straight configuration (zero sweep at the quarter-chord line), a tapered shape, and no twist.

The experimental investigation included three distinct configurations: the isolated wing model, the model incorporating both the wing and the nacelle, and the complete wing, nacelle, and propeller system. These tests aimed to quantify the individual effects of each component. The configuration of the model tested is visually represented in Figure 7.6.

The lift and drag coefficients are the most crucial indicators of the performance of an aircraft. The integrated lift coefficient is plotted against the AoA in Figure 7.11a. Figure 7.11b displays the validation of CL vs CD polar against experimental data from [45]. The lift and drag values obtained from FlightStream were calculated using the Kutta-Joukowski theorem. A 10.4% difference was found in the CL obtained from FlightStream compared to wind tunnel tests. At $CL = 0.8$, FlightStream predicted CD within 12.34% of the experimental results. The error in lift and drag is likely due to modeling error since FlightStream uses a potential flow model and iteratively develops the boundary layer using a suitable boundary layer model. The error in drag is a combination of the error in

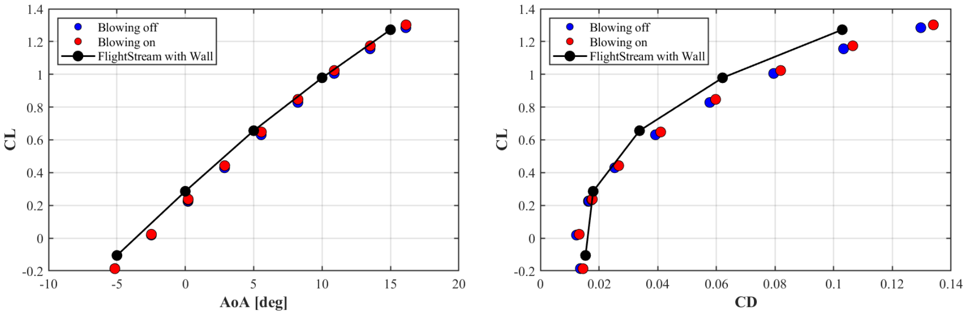

(a) Validation of isolated wing lift polar

(b) Validation of isolated wing drag polar

Figure 7.11: Validation of the numerical model for prediction of integrated lift and drag polars (isolated wing) against experimental data [45]

induced drag and profile drag. FlightStream uses the boundary layer model to develop the boundary layer over potential flow solutions, and the induced drag is calculated as the lift-induced drag due to the model with the boundary layer. Profile drag is predicted using analytical equations applied with the boundary layer properties obtained from the developed boundary layer.

7.5. VALIDATION OF PROPELLER-WING SYSTEM

The propeller-wing system used to validate FlightStream against is chosen from the same source as that used for the isolated wing validation. The geometry used is presented in Figure 7.6. The experimental study was conducted in the Low-Speed Tunnel of the German-Dutch Windtunnels, featuring a 3m by 2.2m test section and a maximum velocity of 80m/s. The setup includes a tapered wing model with a NASA MS-0317 airfoil and a 6-bladed propeller (TUD-XPROP), both mounted on a balance to measure aerodynamic forces, and equipped with pressure taps and microphones for detailed analysis of the forces and flow conditions.

As previously stated in section 7.4, the integrated lift and drag coefficients are the crucial parameters for this study. The lift and net axial force (CX) polars are validated against [45] and are presented in Figure 7.12. A 10.7% error in the CL value was observed at an angle of attack (AoA) of 5 degrees. However, a 16.3% error was noted in the net axial force coefficient at CL=0.6. These errors were attributed to three factors. Firstly, during the wind tunnel test, the propeller was integrated into the wing through an axisymmetric nacelle. However, in the numerical study using FlightStream, the nacelle was not taken into consideration. The nacelle's blocking effect would result in a greater profile drag. Secondly, the errors in modeling the propeller and wing using the vortex panel method coupled with the boundary layer model, as compared to experiments, also contributed to the overall errors.

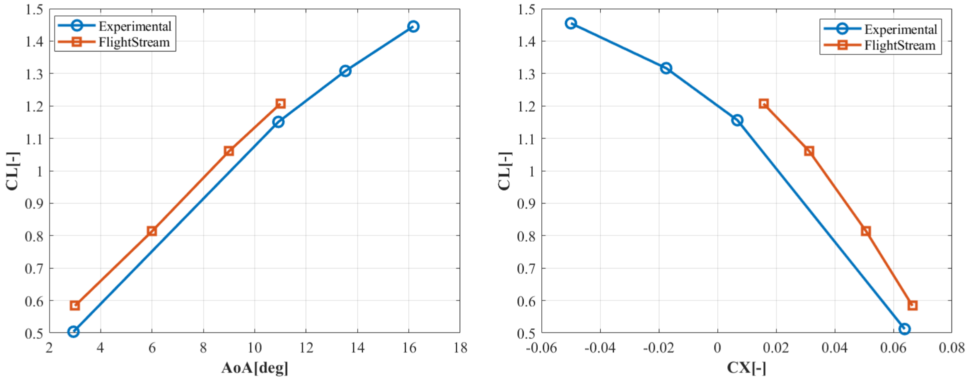

(a) Validation of system lift polar

(b) Validation of net axial force coefficient (CX) polar

Figure 7.12: Validation of the numerical model for prediction of integrated lift and axial force polars (propeller-wing system) against experimental data [45]

Within the scope of this thesis, a comparative study is conducted, comparing two different systems. Therefore, the relatively higher errors can be accommodated within the thesis's scope.

8

RESULTS

In this chapter, the primary objective is to provide answers to the research questions that were initially formulated in the earlier sections of the report. The investigation begins by considering a single propeller configuration where the propeller is positioned at 30% of the wingspan, based on the ATR 42/300 aircraft. This configuration is referred to as "system 1" and is illustrated in Figure 8.1a. It is compared with "system 2," depicted in Figure 8.1b.

This chapter commences with an overview of the performance metrics used for comparison. Subsequently, it delves into a discussion of the operating conditions, encompassing aspects such as the propeller operating point and the wing angle of attack. The chapter then provides a comprehensive analysis of the aerodynamic performance of both single and multi-propeller systems. This analysis encompasses key areas such as lift distribution, induced drag distribution, and a comparative assessment of different systems.

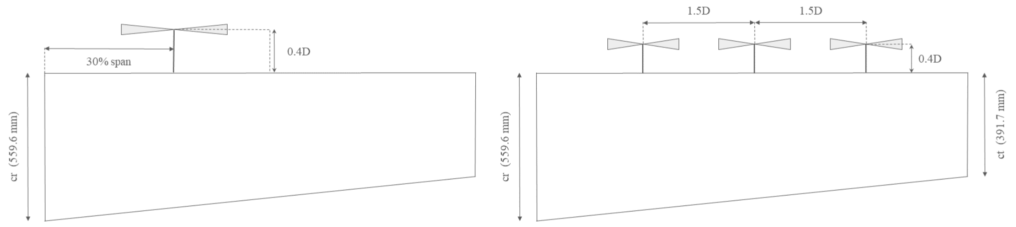

(a) System 1

(b) System 2

Figure 8.1: Planform view of the two systems compared in this thesis

8.1. PERFORMANCE METRICS FOR COMPARISON

The performance metrics typically used for comparing propeller wing systems are the wing lift-to-drag ratio (CL/CD) and propeller propulsive efficiency (η_p). However, as Cole et al. [23] highlighted in their 2021 paper, these metrics are not entirely adequate for evaluating the overall performance changes in propeller wing systems. For instance, the lift-to-drag ratio of the system does not account for the variations in propeller efficiency caused due to the interaction. Likewise, the impact of altered propeller performance on wing performance is not considered. This oversight implies that a decrease in propeller efficiency could lead to a decline in overall system performance as will be described in greater detail in subsection 8.2.1 and vice-versa. Therefore, it is crucial to establish performance metrics that evaluate both individual components (wing and propeller) and the propeller-wing system as a whole.

To address this, the approach outlined by Cole et al. [23] is followed. This method utilizes the propeller power required for steady-level flight as a benchmark for comparing different propeller-wing systems. In steady-level flight, the forces acting in each direction are balanced and equal to zero, meaning thrust equals drag, and lift equals weight. In this thesis, steady-level flight conditions are considered solely based on the propeller and wing, disregarding the lift and drag contributions from other components like the fuselage and empennage. The steady-level flight condition is achieved through the use of two non-dimensional coefficients, namely CX and CL_{sys}, which are further elaborated in Equation 8.1 and Equation 8.2. In this the steady-level flight conditions are defined as $CX = 0$ and $CL_{sys} = 0.5$. As said before, the contribution and interactive influence of the rest of the aircraft are not taken into consideration within the scope of this thesis.

$$CX = \frac{T\cos(\alpha_t) - D}{(1/2)\rho V_\infty^2 S_w} \tag{8.1}$$

$$CL_{sys} = \frac{T\sin(\alpha_t) + L}{(1/2)\rho V_\infty^2 S_w} \tag{8.2}$$

Once this condition is imposed and achieved, three different parameters are calculated to effectively evaluate and compare systems. These parameters are: $\left(\frac{CL}{CD}\right)_{wing}$, η_P, and C_P. Where $C`P$ is the propeller power required to maintain the above-stated steady-level flight conditions. The $\left(\frac{CL}{CD}\right)_{wing}$ and η_P are compared across systems as well as with the isolated wing and the isolated propeller.

8.2. OPERATING CONDITIONS

8.2.1. PROPELLER OPERATING POINT

A previous parametric study on propeller-wing systems [32] studied the influence of various operating points of the propeller on the performance of propeller-wing systems. The major takeaway from the study was that increasing tangential velocity in the propeller slipstream (swirl) leads to increasing positive swirl recovery and leads to a net positive effect on the wing performance. However, increasing swirl in the propeller slipstream implies a greater loss in propeller efficiency as the tangential component does not contribute to the thrust produced by the propeller. Thus, although the performance of the

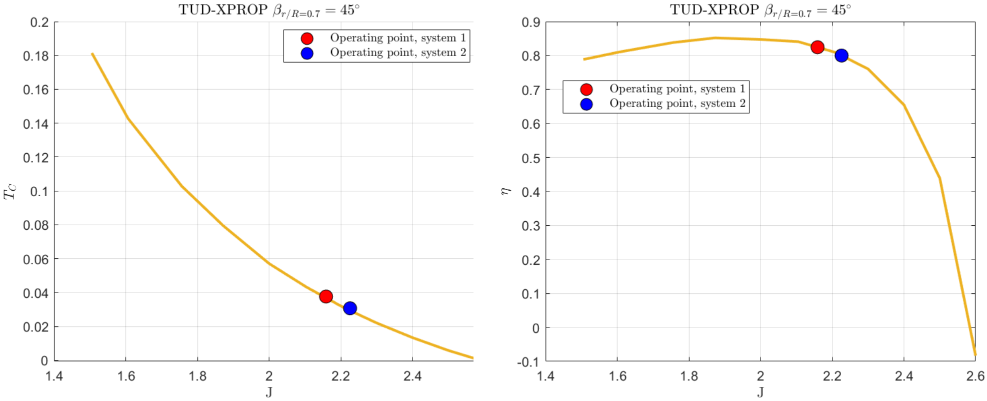

(a) T_C curve showing propeller operating points in system 1 and system 1

(b) η curve showing propeller operating points in system 1 and system 1

Figure 8.2: Propeller operating point in System 1 and System 2

wing increases with increasing swirl, the propeller performance drops. It was observed that the net performance of the system drops from an increase in propeller swirl. Hence, in this study, it is attempted to keep the propeller operating close to the maximum efficiency point as much as possible, such that the normal to tangential velocity ratios remain realistic.

However, it's important to note that the pitch angle of the propeller remains constant at 45° throughout this thesis. This choice is made because conducting a comprehensive analysis involving various pitch angle and advance ratio sweeps would require a multitude of simulations to achieve the desired CX and CL, all while keeping the propeller at its optimal operating point.

For reference, the propeller operating points for both System 1 and System 2 are detailed in Figure 8.2

8.3. SINGLE-PROPELLER SYSTEM

For the single propeller system, the final operating point was obtained at $J = 2.057$ and $\beta = 45^\circ$. The spanwise wing lift and drag distribution with the propeller operating at $\beta = 45^\circ$ is presented in Figure 8.3. The rotational direction of the propeller is inboard-up.

8.3.1. LIFT DISTRIBUTION

As can be seen in Figure 8.3a, the spanwise lift distribution is affected not only in the slipstream-washed region but also in the area outside the slipstream due to changes in lift within the slipstream, which alter the circulation gradient outside the slipstream washed region as well.

The propeller's slipstream has a significant impact on lift, primarily in regions 2 and 3. Because the propeller operates with an inboard upward orientation, region 2 experiences an upwash as it is on the upward-going blade side of the propeller. This upwash directly influences lift in this region by increasing the local angle of attack. Conversely, region 3, being on the downward-going blade side of the propeller, experiences a downwash that results in a decrease in the local angle of attack, directly reducing lift in this region. Additionally, both regions 2 and 3 also experience an increase in lift due to the increase in axial momentum in the slipstream.

The lift in regions 1 and 4 is indirectly influenced by the propeller due to alterations in circulation distribution within the slipstream-affected region.

The propeller creates this circulation gradient between the propeller-washed region and the region outside the propeller-washed area. Consequently, vortex filaments are generated, leading to the induction of upwash and downwash velocities in regions 1 and 4, respectively. This, in turn, causes an increase and decrease in lift when compared to the isolated wing case, as demonstrated in Figure 8.3a.

8.3.2. INDUCED DRAG DISTRIBUTION

In the context of propeller-wing systems, induced drag, as discussed in this report, has two components. One component arises from the lift distribution on the wing, while the other results from the swirl in the slipstream of the propeller. For clarity, the induced drag due to the lift distribution is referred to as circulation-induced drag, and the induced drag due to slipstream swirl is termed swirl recovery. Note that further breakdown of induced drag into these components is not within the scope of this thesis.

The red line in Figure 8.3a illustrates the lift distribution on an isolated wing lift coefficient of 0.5. For the isolated wing, the lift distribution is such that the spanwise lift coefficient gradient, $\frac{dCl}{dy}$, is zero or mildly positive in regions 1, 2, and 3. The gradient turns negative beyond this point towards the wingtip. However, under the influence of the propeller, the gradient becomes more positive in region 1 and partially in region 2, as shown by the black curve. This positive gradient indicates an increase in circulation. As per the Helmholtz theorem, this leads to an upwash in the inboard region of the wing, resulting in a reduction in circulation-induced drag. This reduction is reflected in the dip in induced drag in Figure 8.3b, observed partly in region 1 and partly in region 2.

In region 4, the majority of the wingspan experiences a slight increase in induced drag for both the isolated wing and the system wing, driven by the negative gradient in lift distribution, resulting in a proportional increase in circulation-induced drag. However, the drag in this region still remains lower for the system wing than the isolated wing due to a slightly larger lift gradient observed in the isolated wing.

Regions 2 and 3 fall directly under the influence of the slipstream, and as a result, both the induced drag due to the circulation gradient and the effects of swirl recovery contribute to the total induced drag in these regions.

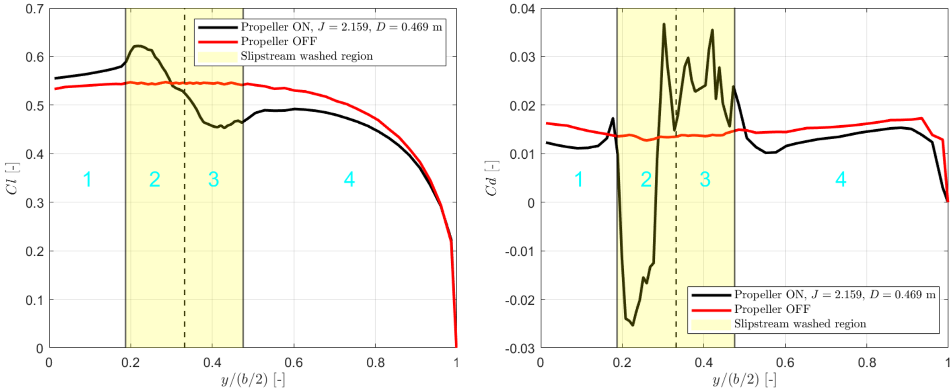

(a) Spanwise wing lift distribution for a system $Cl = 0.5$ compared with wing isolated wing lift distribution for $Cl = 0.5$

(b) Spanwise wing drag distribution for a system $Cl = 0.5$ compared with wing isolated wing drag distribution for $Cl = 0.5$

Figure 8.3: TUD-XPROP propeller

In the initial segment of region 2, a strong negative gradient in induced drag is observed because of the positive circulation gradient. This positive circulation gradient induces an upwash in the inboard region of the wing, causing the resultant lift vector to tilt forward. Concurrently, the propeller-induced upwash is most pronounced at the blade tip and diminishes as one moves away from the tip. Consequently, this creates a negative gradient in swirl recovery in this area. However, the absolute values of induced drag reach a minimum here due to the combined impact of both reduction in circulation-induced drag and positive swirl recovery.

Moving on to the latter portion of region 2, a highly positive gradient in induced drag is observed due to the significant vortex shedding resulting from the pronounced negative spanwise gradient in circulation. This vortex shedding induces a downwash, leading to a backward tilt of the lift vector and, consequently, an increase in induced drag. Additionally, the strong positive gradient in induced drag can also be attributed to the diminishing propeller-induced upwash velocities, causing a decrease in swirl recovery on the up-rotating blade side as we move towards the blade root.

In the initial half of region 3, induced drag increases and reaches its peak due to the negative gradient in circulation in this region, combined with the decreasing swirl recovery resulting from increased downwash across the down-rotating blade side of the wing. It's worth noting that the absolute value of the peak induced drag in this region is lower than the peak reduction in induced drag observed in region 2. This is due to the change in gradient direction at the slipstream boundary, which induces an upwash inboard of this region. This upwash slightly mitigates the impact of negative swirl recovery in this area.

The remaining part of region 3 experiences a negative gradient in induced drag due to the decreasing gradient-induced drag caused by the positive circulation gradient, resulting in upwash. This upwash effectively rotates the lift vector forward, thus reducing induced drag.

8.3.3. SYSTEM 1 VS. ISOLATED WING

In this section, a comparison is made between two systems: the isolated wing and the propeller-wing system featuring a single propeller placed approximately 30% of the wing's length from the root. Both systems are set to have a net system force in the lift and drag directions (CL and CX) fixed at 0.5 and 0, respectively. The evaluation of these two systems' performance relies on the wing lift-to-drag ratio (CL/CD), and the results are presented in Table 8.1. The table also provides a comparison of wing lift, induced drag, viscous drag, and total drag for both systems.

It should be noted that the lift coefficient of the system's wing is lower than the prescribed 0.5 because the system's lift coefficient includes the component of propeller force in the lift direction, as discussed in section 8.3. The propeller slipstream affects the induced drag of the wing both directly (swirl recovery) and indirectly (by altering the circulation distribution over the entire wing). However, the detailed breakdown of induced drag components within this thesis is beyond the scope.

Nevertheless, it is evident that with the same system lift and x-force coefficients, the total induced drag of the wing is significantly reduced (-21.21%). Apart from the induced drag components, the rotation of the lift vector backward due to induced velocities is also smaller, attributed to the lower wing lift coefficient. However, the zero-lift drag (CD_o) increases due to an increase in skin friction drag within the propeller slipstream. This effect is axisymmetric, as axial momentum increases on both the up-rotating and down-rotating blade sides. In summary, the reduction in induced drag is more pronounced than the increase in zero-lift drag, resulting in a 10.12% reduction in total wing drag. Consequently, the lift-to-drag ratio of the wing in the two systems improves by 9.57%, signifying a substantial enhancement in wing performance.

8.3.4. PROPELLER PEFORMANCE IN SYSTEM 1

Turning attention to the impact on propeller performance, an isolated propeller is simulated, generating thrust equal to the wing drag in the single propeller-wing system. The operating point of the isolated propeller, at which it generates the required thrust, is marked in Figure 8.4. It is evident that the system propeller benefits from the propeller-wing interaction, achieving a 3.85% greater efficiency compared to the isolated propeller producing the same thrust. However, it's important to consider that the system propeller does not operate at the same advance ratio as the isolated propeller, which means the isolated propeller is already operating at a suboptimal point. To make a fair comparison, one would need to iteratively adjust the propeller pitch angle and advance ratio in both the system and isolated cases to ensure each operates at the most optimal point. Nonetheless, efforts have been made to keep the propeller operating point as close to the optimal point as possible.

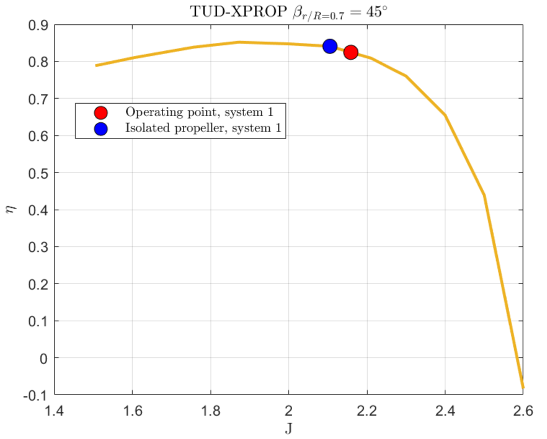

Figure 8.4: Propeller operating point in system 1 and isolated propeller with same T_c

Table 8.1: System 1 vs Isolated wing

	Isolated Wing	**System Wing**	Δ
CL	0.499	0.492	-1.52%
CDi	0.0132	0.0104	-21.21%
CDo	0.0122	0.0126	3.27%
CD	0.0254	0.0229	-10.12%
CL/CD	19.62	21.50	9.57%

Table 8.2: System 1 Propeller performance

	J	**TC**	**PC**	η
Isolated Propeller	2.105	0.0404	0.0489	0.827
System Propeller	2.159	0.0404	0.0471	0.859
Δ			-3.70%	3.86%

8.4. MULTI-PROPELLER SYSTEM

8.4.1. LIFT DISTRIBUTION

Figure 8.5a and Figure 8.5b depict the lift and drag distributions respectively for the multiple propeller system. The lift distribution within the boundary of the propeller slipstream of each propeller can be explained in a manner consistent with what was discussed in section 8.3. However, there is a notable difference for the first two inboard propellers. In these cases, the dip in lift behind the down-rotating blade side is not as pronounced as observed in the single propeller system. This difference can be attributed to the presence of the up-rotating blade of the adjacent propeller, which results in a stronger positive gradient in lift at the slipstream boundary. This stronger positive gradient has a beneficial effect on induced drag because it reduces the peaks in induced drag experienced by the system wing located behind these two inboard propellers. Further details on this topic are provided in subsection 8.4.2.

8.4.2. INDUCED DRAG DISTRIBUTION

The induced drag distribution is analyzed similarly to what was explained for the induced drag distribution of the wing in the single propeller system. The induced drag comprises two components: circulation gradient-induced drag and swirl recovery induced by the propeller. The influence of swirl recovery is primarily observed within the boundaries of the slipstream-affected region behind each propeller. The trends in gradients, maxima, and minima of these components follow the same pattern as explained for the single propeller case in subsection 8.3.2.

However, at the interface of the slipstream boundary for the two inboard propellers, a stronger positive gradient in lift, resulting from the up-rotating blade of the adjacent propeller, leads to a less significant dip in the lift coefficient behind these inboard propellers. This results in a smaller peak in induced drag coefficient because the stronger positive gradient in lift implies a more pronounced upwash (reduced total downwash) in the region inboard to this, which subsequently reduces circulation-induced drag. This is shown in the illustration in Figure 8.6b. This illustration shows the force diagram for a section of the wing that lies in the downgoing blade side of the inboard propeller such that it experiences the effect of the increase in lift gradient at the slipstream boundary due to the uprotating blade of the adjacent propeller. The increase in lift gradient will result in an additional upwash, $V_{circ,adj}$ that will reduce the impact of the initial downwash experienced by the section. This will increase the effective angle of attack seen by this section, as compared to the case with a single propeller. This leads to a greater forward rotation of the enlarged lift vector, leading to lesser induced drag compared to a single propeller configuration.

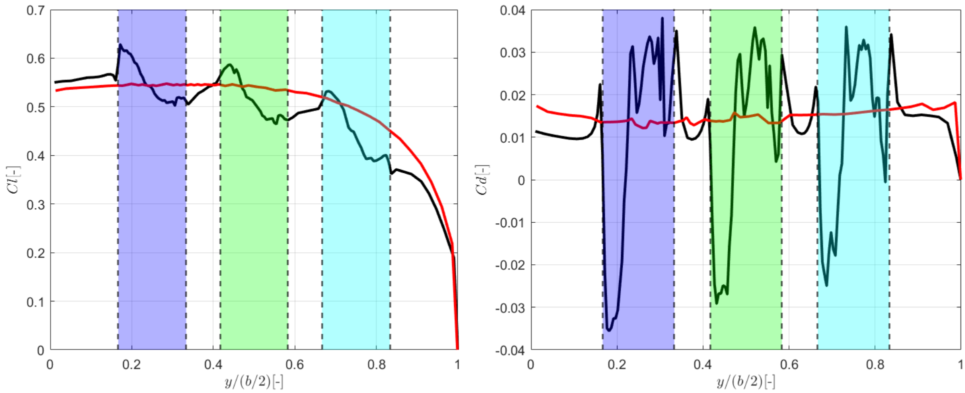

(a) Spanwise wing lift distribution for a system $Cl = 0.5$ compared with wing isolated wing lift distribution for $Cl = 0.5$

(b) Spanwise wing drag distribution for a system $Cl = 0.5$ compared with wing isolated wing drag distribution for $Cl = 0.5$

Figure 8.5: Multiple propeller system: Spanwise lift and drag distributions

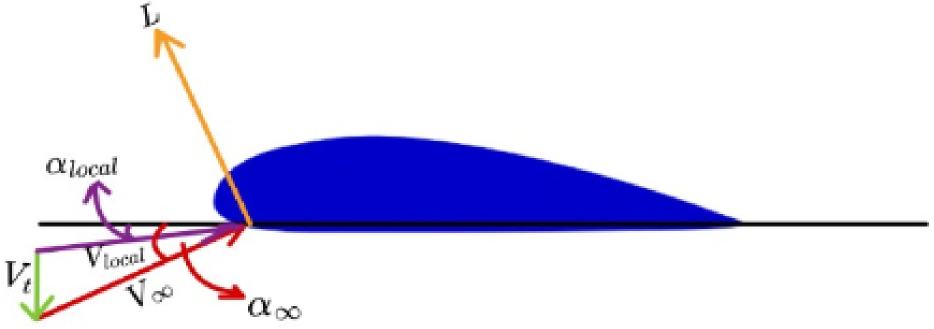

(a) Force diagram for a section of the wing in the downgoing blade side for a single propeller configuration

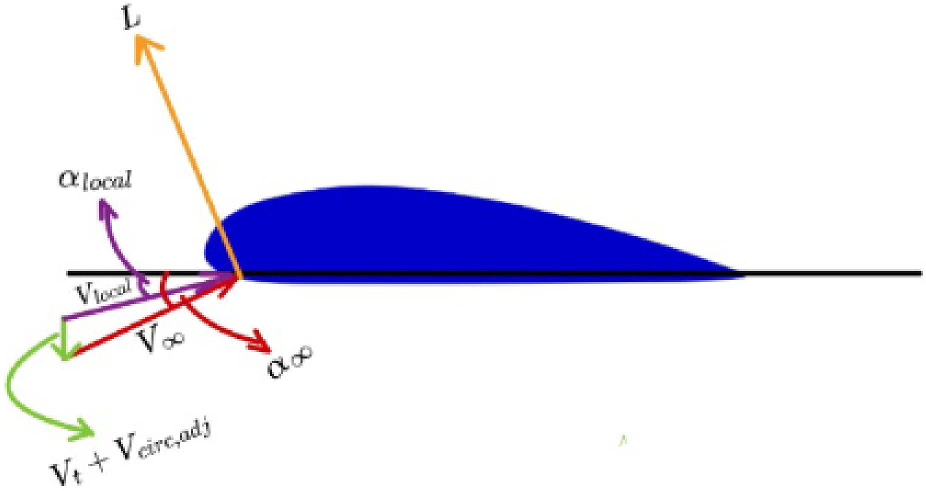

(b) Force diagram for a section of the wing in the downgoing blade side of the inboard propeller in a multiple propeller configuration

Figure 8.6: Illustration to show the effect of the adjacent propeller on the wing section behind an inboard propeller

8.5. SYSTEM 2 VS. ISOLATED WING

In this section, a comparison is conducted between the isolated wing and the leading-edge distributed propeller-wing system featuring three tractor propellers. Similar to the single propeller system, for the sake of a fair comparison, the system is configured to have a net system force in the lift and drag directions (CL and CX) fixed at 0.5 and 0, respectively. Once again, the parameter used for assessing the interactive advantages of the propeller-wing system on the wing is the wing lift-to-drag ratio.

From the data presented in Table 8.3, it becomes evident that the interaction between the propellers and the wing in system 2 yields significant benefits in terms of reducing the induced drag of the wing (CD_i), which decreases by 26.5%. This reduction is highly noteworthy. However, it's important to note that the profile drag (CD_o) experiences a modest increase of 2.46%. This increase can be attributed to an overall increase in axial momentum on both the upgoing and downgoing blade sides.

Nonetheless, despite the increase in profile drag, the total drag (CD) decreases by 12.87%, resulting in a 14.1% increase in the wing's lift-to-drag ratio. This improvement in the wing's lift-to-drag ratio is substantial and highlights the advantages of the propeller-wing system on the wing performance.

8.5.1. PROPELLER PERFORMANCE IN SYSTEM 2

To assess the interactive benefits on each of the propellers, the propeller efficiencies are compared with that of an isolated propeller. The isolated propeller is operated in such a way that the thrust coefficient (T_c) produced by the isolated propeller matches the average thrust coefficient of the three propellers in the system. This approach ensures a fair comparison and allows for a comprehensive evaluation of the interactive advantages on the propellers.

The performance parameters for each of the three propellers in the system, as well as the isolated propeller, are presented in Table 8.4. Notably, the efficiency of the most inboard placed propeller exhibits the most significant increase ($\Delta\eta = 7.52\%$) compared to the other outboard propellers. The middle propeller experiences the least benefit due to the propeller-wing interaction, with an efficiency increase of ($\Delta\eta = 6.07\%$). Meanwhile, the most outboard placed propeller demonstrates an efficiency increase of ($\Delta\eta = 6.87\%$) due to the interactive benefits with the propeller-wing system. Once again, these results are to be taken with a pinch of salt as the isolated propeller is not operating at the most optimal point as shown in Figure 8.7

Table 8.3: System 2 vs isolated wing

	Isolated Wing	**System Wing**	Δ
CL	0.499	0.489	-2.1%
CDi	0.0132	0.0097	-26.5%
CDo	0.0122	0.0125	2.46%
CD	0.0255	0.0222	-12.87%
CL/CD	19.32	22.04	14.10%

8.5.2. SYSTEM 1 VS. SYSTEM 2

In the preceding sections, the comparison between the propeller-wing systems (System 1 and System 2) and isolated wings and propellers was elaborated upon. The final step involves a comparison between the two propeller-wing systems themselves, namely the single propeller system and the distributed propeller system. This comparison is based on evaluating the power coefficient required for maintaining steady-level flight

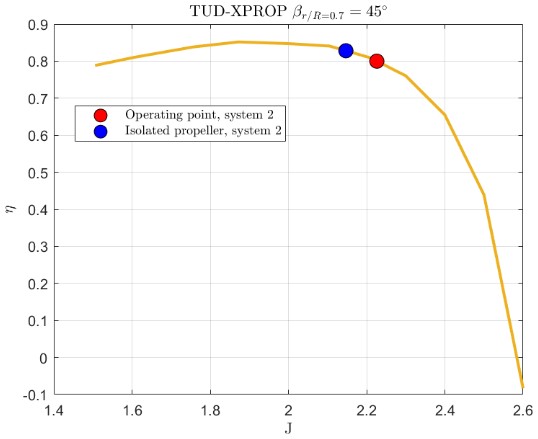

Figure 8.7: Propeller operating point in system 2 and isolated propeller with average T_C of the 3 propellers

Table 8.4: System 2 Propeller performance

	TC	**PC**	η	$\Delta\eta$
P_1	5.758	0.0434	0.8850	6.87%
P_0	5.586	0.0424	0.8784	6.07%
P_{-1}	5.878	0.0440	0.8904	7.52%
Isolated propeller	5.740	0.0456	0.8281	

with $CX = 0.5$ and $CL = 0.5$ for each system, and calculating the difference.

For the single propeller system, the analysis reveals that the power coefficient required to sustain steady-level flight is $CP_{sys1} = 0.047$, whereas for the distributed propeller system, it is found to be $CP_{sys2} = 0.043$. Consequently, the leading-edge distributed propeller-wing system demands 8.1% less power than the single propeller-wing system.

To elucidate this disparity, an examination of the interactive benefits on each component within the respective systems is warranted. Initially, the performance of the wing is scrutinized. Data presented in Table 8.1 and Table 8.3 indicates that the wing within the distributed propeller system exhibits a 3% increase in efficiency (CL/CD). This remarkable enhancement is attributed to a noteworthy 6.1% reduction in induced drag.

Furthermore, a comprehensive analysis of the interactive benefits on the propellers is essential. On average, a propeller in the distributed system experiences a 3% increase in efficiency compared to the propeller in System 1. Consequently, the cumulative impact of interactive benefits on both the wing and propeller components significantly contributes to the distributed propeller system (System 2) demonstrating superior efficiency in comparison to System 1.

9

CONCLUSION AND RECOMENDATIONS

9.1. CONCLUSION

This thesis investigated propeller-wing interaction aerodynamics, focusing on leading-edge distributed propeller configurations. Initially, a literature review was conducted, revealing a lack of research in this specific area, especially compared to single leading-edge tractor propulsion systems. It was expected that the induced drag of the wing decreases more in the case of the three propeller system, compared to the single propeller system.

A comparative study was then executed, using a wing and propeller system based on the ATR 42/300 model as the baseline single tractor propeller configuration and a three-propeller leading-edge distributed configuration. For the analysis, an unsteady panel method solver from FlightStream was utilized, allowing for a detailed examination of the two-way interactions between the propeller and wing (Full interaction mode), and ensuring a force-free wake.

Following the approach outlined by Cole et al. [23], this study utilized the propeller power required for steady-level flight as a benchmark for comparing the two propeller-wing systems. This approach, focusing on fixed CX and CL_{sys} coefficients, allowed for a more nuanced evaluation of the systems, considering both individual components and the overall propeller-wing interaction. It was obtained that the 3-propeller leading-edge distributed system consumed 8.1% less power to maintain steady, level-flight conditions compared to the baseline single-propeller system. This indicates the potential for improved efficiency in aircraft designs using such configurations.

The analysis, performed without including the nacelle in either configuration, provided insights into the lift and induced drag distribution. It was found that the leading edge distributed propeller configuration showed aerodynamic benefits over the conventional single propeller configuration, particularly in terms of increased wing efficiency (2.5% better) owing to 6.1% lower induced drag.The decrease in induced drag can be attributed to the reduction in downwash encountered by the wing behind the downgoing blade side of the inboard propellers in the leading-edge distributed configuration. This reduction occurs due to an increase in circulation gradient at the interface between the slipstream boundaries. This heightened circulation gradient is a result of the upgoing blade of the adjacent propeller. Additionally, the propeller efficiency increased by 3% in the leading edge distributed system compared to the single propeller system. However, conclusions on propeller performance need to be taken with a pinch of salt because the propellers were operating at different operating points (different from the most optimal), already leading to a difference in performance.

In summary, this thesis offers a scientific contribution to the field of aerospace engineering, providing new insights into the aerodynamics of leading-edge distributed propeller systems and their potential to enhance aircraft performance.

9.2. RECOMENDATIONS FOR FUTURE WORK

The work done in this thesis, despite providing several meaningful insights into the interactive benefits of propeller-wing systems in a leading-edge distributed configuration, there are several ways in which the study could be improved and expanded.

The current thesis did not include the nacelle in its model, despite its recognized importance in distributed propeller systems, as highlighted by De Vries et al. [49]. Future research could explore the nacelle's impact on the interactive benefits of these systems, offering valuable insights into their overall performance. This addition is essential to understand the full scope of propeller interactions within these complex systems.

In terms of expanding the propeller-wing system analysis, the study was initially limited to contrasting two basic configurations, focusing on one variant of the 3-propeller system through unsteady simulations. Future studies should aim to broaden this scope by integrating a variety of distributed propeller configurations. This expansion can be achieved by utilizing steady-state simulations coupled with simplified propeller models, such as the Blade Element Momentum (BEM) theory or the actuator disc model. By altering and examining the effects of propeller-to-wing spacing, inter-propeller distances, and considering configurations like the staggered arrangement, researchers can comprehensively explore the design space. This approach not only allows for the identification of optimal configurations but also enables a direct comparison with known efficient models, such as tip-mounted propellers. The variation in propeller diameter and its subsequent impact on system performance is another avenue for exploration.

Furthermore, modifying parameters like the net lift coefficient, CL_{sys}, and the net force in the drag direction, CX, under different steady, level-flight conditions, would provide a deeper understanding of the system's dynamics. By identifying the most influential parameters in propeller-wing interactions, the design space for leading-edge distributed propulsion configurations can be effectively constrained. Establishing clear boundaries within this design space is crucial for enhancing the efficiency of multidisciplinary optimization processes. A focused approach in exploring design variables enables more effective optimization and decision-making throughout the design process. This comprehensive methodology ensures a more targeted and efficient exploration of the design space, leading to potentially groundbreaking findings in the field of distributed propeller systems.

BIBLIOGRAPHY

[1] J. D. Anderson. *Fundamentals of Aerodynamics*. 5th. New York: McGraw-Hill, 2011. ISBN: 978-0073398105.

[2] T.C.A. Stokkermans. "Aerodynamics of Propellers in Interaction Dominated Flowfields: An Application to Novel Aerospace Vehicles". PhD thesis. The Netherlands: Delft University of Technology, Nov. 2020.

[3] K. A. Deere et al. "Computational analysis of a wing designed for the X57 distributed electric propulsion aircraft". In: *AIAA Aviation Forum*. American Institute of Aeronautics and Astronautics. June 2017. DOI: `10.2514/6.2017-3923`.

[4] L. L. M. Veldhuis. "Review of Propeller-Wing Aerodynamic Interference". In: *24th International Congress of the Aeronautical Sciences*. 2004.

[5] Robert Deters, Gavin Ananda, and Michael Selig. "Reynolds Number Effects on the Performance of Small-Scale Propellers". In: June 2014. ISBN: 978-1-62410-288-2. DOI: `10.2514/6.2014-2151`.

[6] Robert Nederlof. "Improved Modeling of Propeller-Wing Interactions with a Lifting-Line Approach: Investigation of a Suitable Correction Method to Account for the Finite Slipstream Height". MSc Thesis. Delft University of Technology, 2020. URL: `http://repository.tudelft.nl/`.

[7] L. L. M. Veldhuis. "Propeller Wing Aerodynamic Interference". PhD thesis. Delft University of Technology, June 2005.

[8] Robert Kooij. "Modeling and Performance Assessment of Propeller-Wing Interactions". MSc Thesis Literature Study.

[9] Ilan Kroo. "Propeller-wing integration for minimum induced loss". In: *Journal of Aircraft* 23.7 (July 1986), pp. 561–565. DOI: `10.2514/3.45344`. URL: `https://doi.org/10.2514/3.45344`.

[10] L. J. Heidelberg and R. P. Woodward. "Advanced Turboprop Wing Installation Effects Measured by Unsteady Blade Pressure and Noise". In: *11th Aeroacoustics Conference*. Oct. 1987. DOI: `10.2514/6.19872719`.

[11] N. Van Arnhem and et al. "Aerodynamic Interaction Effects of Tip-Mounted Propellers Installed on the Horizontal Tailplane". In: *AIAA Aerospace Sciences Meeting*. American Institute of Aeronautics and Astronautics Inc. 2018. DOI: `10.2514/6.2018-2052`.

[12] Y. Lei, Wj. Yang, and Yy. Huang. "Aerodynamic performance of distributed electric propulsion with wing interaction". In: *Journal of Zhejiang University Science A* 23 (2022), pp. 27–39. DOI: `10.1631/jzus.A2100192`.

[13] Till K. Lindner et al. “Experimental Propeller Placement Analysis for a Distributed Propulsion Wing Section in High Lift Configuration”. In: *AIAA 2023-3539, Session: Aero-Propulsive Interactions II.* Published Online: 8 Jun 2023. American Institute of Aeronautics and Astronautics. 2023. DOI: 10.2514/6.2023-3539.

[14] Danilo Ciliberti et al. “Aero-Propulsive Interactions between UAV Wing and Distributed Propellers Due to Their Relative Position”. In: *Drones* 7.1 (2023). ISSN: 2504-446X. DOI: 10.3390/drones7010049. URL: https://www.mdpi.com/2504-446X/7/1/49.

[15] R. S. W. Cheung. *Numerical Prediction of Propeller Performance by Vortex Lattice Method.* Technical Note 265. UTIAS, Nov. 1987.

[16] J. J. Bertin and R. M. Cummings. *Aerodynamics for Engineers.* 5th. Pearson Prentice-Hall, 2009. ISBN: 978-0132355216.

[17] G. Bramesfeld. “A Higher Order Vortex-Lattice Method with a Force-Free Wake”. PhD thesis. Pennsylvania State University, Aug. 2006.

[18] Götz Bramesfeld and Mark D. Maughmer. “Relaxed-Wake Vortex-Lattice Method Using Distributed Vorticity Elements”. In: *Journal of Aircraft* 45.2 (Mar. 2008), pp. 560–568. DOI: 10.2514/1.31665. URL: https://doi.org/10.2514/1.31665.

[19] J. A. Cole. “A Higher-Order Free-Wake Method for Aerodynamic Performance Prediction of Propeller-Wing Systems”. PhD thesis. Pennsylvania State University, Dec. 2016.

[20] K. W. Mortara and M. D. Maughmer. “A Method for the Prediction of Induced Drag for Planar and Non-Planar Wings”. In: *AIAA Paper 93-3420.* Aug. 1993.

[21] S. C. Smith and I. Kroo. “Computation of Induced Drag for Elliptical and Crescent-Shaped Wings”. In: *Journal of Aircraft* 30.4 (July 1993), pp. 446–452.

[22] M. A. DeHaan. “Induced Drag of Wings with Highly Swept and Tapered Wing Tips”. In: *AIAA Paper 90-3062-CP.* Aug. 1990.

[23] Julia A. Cole et al. “Higher-Order Free-Wake method for Propeller–Wing systems”. In: *Journal of Aircraft* 56.1 (Jan. 2019), pp. 150–165. DOI: 10.2514/1.c034720. URL: https://doi.org/10.2514/1.c034720.

[24] Danilo Ciliberti et al. “Aero-Propulsive Interactions between UAV Wing and Distributed Propellers Due to Their Relative Position”. In: *Drones* 7.1 (Jan. 2023), p. 49. DOI: 10.3390/drones7010049. URL: https://doi.org/10.3390/drones7010049.

[25] Dave P. Witkowski, Alex K. H. Lee, and John P. Sullivan. “Aerodynamic interaction between propellers and wings”. In: *Journal of Aircraft* 26.9 (Sept. 1989), pp. 829–836. DOI: 10.2514/3.45848. URL: https://doi.org/10.2514/3.45848.

[26] H. M. W. Hoeijmakers. *Panel Methods for Aerodynamic Analysis and Design.* Rept. 783. Neuilly sur Seine, France: Special Course on Engineering Methods in Aerodynamic Analysis and Design of Aircraft, AGARD, 1991.

[27] B. Maskew. *Program VSAERO Theory Document.* CR-4023. NASA, 1987.

[28] W. Johnson. “A General Free Wake Geometry Calculation for Wings and Rotors”. In: *AHS Annual Forum Proceedings.* American Helicopter Society. Fairfax, VA, 1995.

[29] W. Johnson. “Rotorcraft Aerodynamics Models for a Comprehensive Analysis”. In: *AHS Annual Forum Proceedings* 54 (1998), pp. 71–94.

[30] R. M. A. Maretta. “Performance of a Propeller Embedded in the Flowfield of a Wing”. In: *Journal of Aircraft* 33.5 (1996), pp. 919–923. DOI: `10.2514/3.47036`.

[31] J. A. Cole et al. “Influence of Propeller Location, Diameter, and Rotation Direction on Aerodynamic Efficiency”. In: *Journal of Aircraft* 58.1 (2021), pp. 63–71. DOI: `10.2514/1.C035917`.

[32] R. Willemsen. “A Sensitivity Study on the Aerodynamic Performance of a Wingtip-Mounted Tractor Propeller-Wing System”. MA thesis. Delft University of Technology, Nov. 2020.

[33] B. Horsten and L. L. M. Veldhuis. “A New Hybrid Method to Correct for Wind Tunnel Wall- and Support Interference On-line”. In: Oct. 2009, pp. 507–514.

[34] Research in Flight. *FlightStream Quick Start Guide*. Version 2023.2. Research in Flight. 2023. URL: `https://repository.researchinflight.com/quickstart2023.pdf`.

[35] Egon Beyne. “Aerodynamic Analysis of a Propeller-Powered Strut-Braced Wing”. Accessed: 2024-03-08. MA thesis. Delft University of Technology, Dec. 2023. URL: `https://repository.tudelft.nl/islandora/object/uuid:581b8540-d67b-42a0-94cc-0a2523cfd0a9`.

[36] Vivek Ahuja and Brandon L. Litherland. “Comparison of Aerodynamic Analysis Tools Applied to a PropellerBlown Wing”. In: *AIAA Scitech 2023 Forum*. National Harbor: AIAA, Jan. 2023. DOI: `10.2514/6.2023-1753`.

[37] Vivek Ahuja. *FlightStream®: Panel Methods Reimagined*. Presentation at Research in Flight. Available at Research in Flight. 2023. URL: `www.researchinflight.com`.

[38] J.L. Hess. *A fully automatic combined potential-flow boundary-layer procedure for calculating viscous effects on the lifts and pressure distributions of arbitrary three-dimensional configurations*. Tech. rep. MDC J7491. Long Beach, California: Douglas Aircraft Company, Aug. 1977.

[39] Vivek Ahuja, Roy Hartfield Jr., and Danilo Ciliberti. “Three-dimensional Viscous Coupling Flow Separation Enhancements to an Inviscid Surface Vorticity Flow Solver”. In: *AIAA SciTech 2023*. Research in Flight, University of Naples “Federico II”. American Institute of Aeronautics and Astronautics. Austin, Texas, USA; Naples, Italy, 2023. DOI: `10.2514/6.2023-2455`.

[40] B. Thwaites. “Approximate Calculation of the Laminar Boundary Layer”. In: *The Aeronautical Quarterly* 1.3 (1949), pp. 145–280. DOI: `10.1017/S0001925900000184`.

[41] N.M. Standen. *Calculation of integral parameters of a compressible turbulent boundary layer using a concept of mass entrainment*. Tech. rep. 64-14. Montreal: McGill University, 1964.

[42] Frank A. Dvorak, Brian Maskew, and Frank A. Woodward. *Investigation of Three-Dimensional Flow Separation on Fuselage Configurations*. Tech. rep. USAAMRDL-TR-77-4. Bellevue, Washington: Analytical Methods, Inc., 1977.

[43] Stephen C. Smith and Ilan M. Kroo. "Computation of induced drag for elliptical and crescent-shaped wings". In: *Journal of Aircraft* 30.4 (May 1993), pp. 446–452. ISSN: 00218669. DOI: 10.2514/3.46365.

[44] M. C. Towne et al. "PAN AIR modeling studies". In: *AIAA Applied Aerodynamics Conference*. Danvers, Massachusetts: American Institute of Aeronautics and Astronautics (AIAA), July 1983. DOI: 10.2514/6.1983-1830. URL: http://arc.aiaa.org.

[45] Tomas Sinnige and Biagio Della Corte. *Validation of a key technology to TRL4*. Technical Report D5.3. FUTPRINT50 project under the European Union's Horizon 2020 research and innovation programme, grant agreement No 875551. Delft University of Technology; University of Stuttgart; University of Niccolò Cusano, 2023.

[46] B. Della Corte, L. L. M. Veldhuis, and T. Sinnige. *Experimental Aerodynamic Investigation of a Wing with a Tip-mounted Tractor Propeller at Positive and Negative Thrust*. Technical Report. Delft, The Netherlands: Faculty of Aerospace Engineering, Delft University of Technology, 2023.

[47] Q. Li et al. "Design and Experimental Validation of Swirl Recovery Vanes for Propeller Propulsion Systems". In: *AIAA Journal* 56.12 (2018), pp. 4719–4729. DOI: 10.2514/1.J057113.

[48] N. van Arnhem, R. Vos, and L. L. M. Veldhuis. "Aerodynamic Loads on an Aft-Mounted Propeller Induced by the Wing Wake". In: *AIAA Scitech 2019 Forum*. 2019-1093. Jan. 2019. DOI: 10.2514/6.2019-1093.

[49] Reynard de Vries et al. "Aerodynamic interaction between propellers of a distributed-propulsion system in forward flight". English. In: *Aerospace Science and Technology* 118 (2021). ISSN: 1270-9638. DOI: 10.1016/j.ast.2021.107009.